Cement and Concrete Composites 134 (2022) 104808

Contents lists available at ScienceDirect

Cement and Concrete Composites

journal homepage: www.elsevier.com/locate/cemconcomp

Material characterization and piezoresistive sensing capability assessment of thin-walled CNT-embedded ultra-high performance concrete

Joonho Seo [a], Daeik Jang [a], Beomjoo Yang [b], H.N. Yoon [a,c], Jeong Gook Jang [d,*], Solmoi Park [e], H.K. Lee [a]

[a] Department of Civil and Environmental Engineering, Korea Advanced Institute of Science and Technology (KAIST), 291 Daehak-ro, Yuseong-gu, Daejeon, 34141, Republic of Korea
[b] School of Civil Engineering, Chungbuk National University, 1 Chungdae-ro, Seowon-gu, Cheongju, Chungbuk, 28644, Republic of Korea
[c] Applied Science Research Institute,Korea Advanced Institute of Science and Technology (KAIST), 291 Daehak-ro, Yuseong-gu, Daejeon, 34141, Republic of Korea
[d] Division of Architecture and Urban Design, Urban Science Institute, Incheon National University, 119 Academy-ro, Yeonsu-gu, Incheon, 22012, Republic of Korea
[e] Department of Civil Engineering, Pukyong National University, 45 Yongso-ro, Nam-gu, Busan, 48513, Republic of Korea

ARTICLE INFO

Keywords:
Thin-walled CNT
Ultra-high performance concrete
Hydration
Electrical conductivity
Piezoresistive sensing

ABSTRACT

The present study performed material characterization and assessed the piezoresistive sensing capabilities of thin-walled carbon nanotube (TWCNT)-embedded ultra-high performance concrete (UHPC). TWCNTs were incorporated into UHPC from 0 to 0.5% by cement mass. The fresh-state behavior of the samples degraded as the TWCNT content increased. The TWCNT content lower than 0.2–0.3% induced a nucleation effect in the samples; nevertheless, the TWCNT content exceeding this range hindered the hydration. The degree of autogenous shrinkage of the samples proportionally decreased with the TWCNT content owing to the hindered hydration and nano-reinforcing effect of TWCNTs. The electrical percolation threshold range was found to be approximately 0.2% in the TWCNTs, which was further proven by the notable FCR variations in the sample with TWCNT of 0.2% upon cyclic loading test. TWCNTs exceeding the percolation threshold level exhibited stable FCR values regardless of the extent of compressive loading, loading frequency, and number of loading cycles.

1. Introduction

Nearly three decades have passed since the introduction of ultra-high performance concrete (UHPC), which is considered to be tailored to the needs of specific sites where high mechanical properties are required [1–3]. The mixture proportions of UHPC typically use water-to-binder ratios lower than 0.25 and chemical agents such as water-reducers to exhibit high packing density levels, thereby showing superior mechanical properties [4]. Generally, UHPC undergoes a steam-curing process for rapid strength gain, and in this case, compressive strengths higher than 150 MPa have been developed [5]; however, compressive strengths of approximately 120 MPa can be achieved through an ambient curing process [6]. In addition, UHPC exhibits high durability because it is nearly impossible for deteriorating or harmful substances to penetrate its surface [7]. The incorporation of high-volume fibers into UHPC is commonly adopted for practical applications that enable the development of high flexural strength and strain-hardening behavior, even after concrete failure [8]. On the one hand, the active development of water-reducing agents facilitated UHPC to have fine workability and self-compacting properties, becoming very suitable for on-site or large-scale construction [3].

As one of the methods for rendering electrical conductivity to cementitious materials, the incorporation of carbon-based materials has been introduced over the years as the most feasible and effective way [9–13]. The incorporation of carbon-based materials into cementitious materials can dramatically improve their electrical conductivity, enabling the use of these materials for electrical heating, piezoresistive sensors, and electromagnetic shielding composites [14,15]. Among the conductive materials used for cementitious materials, carbon nanotubes (CNTs) are considered the most preferred and highly efficient materials even at low dosages [16]. CNTs have a high aspect ratio and excellent electrical conductivity and are widely used as nano-reinforcements in

* Corresponding author.
E-mail address: jangjg@inu.ac.kr (J.G. Jang).

https://doi.org/10.1016/j.cemconcomp.2022.104808
Received 13 June 2022; Received in revised form 18 September 2022; Accepted 9 October 2022
Available online 17 October 2022

construction materials. Thus, CNTs are considered innovative and are anticipated to act as electrically conductive fillers in cementitious materials.

Jung et al. [16] assessed the dispersion of CNT and mechanical properties of CNT-incorporated UHPC, experimentally proving that the strength enhancement was highest in the sample containing 0.5 wt% of CNT and that the CNT content exceeding 0.5 wt% rather reduced the strength. In addition, the flexural strength of UHPC was found to be increased by the incorporation of CNT [17]. Meanwhile, Jung et al. [18] postulated that the reaction degree of clinker in UHPC was somewhat lowered by the incorporation of CNT, while degree of Al in C-(A)-S-H was slightly increased. On the other hand, Hardy et al. [19] revealed the reduction in the mechanical strength of UHPC due to the agglomeration of incorporated carbon nanomaterials. The conductive network formed in cementitious materials with the aid of CNTs enables the monitoring of structural damages in various construction sectors [20]. The conductive network in cementitious materials can be altered upon exposure to external loadings or cracks [15]. Upon exposure to external loadings, the distances between conductive fillers become physically closer, and vice versa happens when unloading [20]. In this regard, the electrical resistance of the composites becomes reduced and increased upon loading and unloading, respectively [15]. The differences in the electrical resistance can allow one to estimate the applied external loadings [21]. Especially, incorporation CNT was found to be the most effective in exhibiting self-sensing capability than graphite or graphene at an identical volume fraction [22]. This principle can be utilized to make these materials act as piezoresistive sensors [15]. Yu and Kwon [23] synthesized cementitious materials with CNT content of 0.1% and experimentally showed the electrical resistance changes of 9.5 and 11.4% upon loading at 5.2 and 8.6 MPa, respectively, proving the possibility of using cementitious materials as piezoresistive sensors in the construction industry. Nam et al. [24] conducted a vehicle loading test on CNT-embedded cementitious materials to evaluate their potential for use as traffic sensors. Kim et al. [25] demonstrated that the cementitious materials containing 0.5% CNTs were able to exhibit an electrical resistance change of 25% upon exposure to 10 MPa of compressive loadings.

Thin-walled CNTs (TWCNTs) are emerging conductive materials with properties distinct from those of widely used CNTs (multi-walled (MW) or single-walled (SW) CNTs). The diameter and number of walls of TWCNTs are in the range of 4–9 nm and 3–7, respectively, which are larger than those of SWCNTs and smaller than those of MWCNTs. In addition, the cost of TWCNTs in the South Korea is approximately 70.7 $/kg, while that of SWCNTs and MWCNTs are approximately 235.5 $/g and 78.6 $/kg, respectively. In addition to the cost-effectiveness of TWCNTs, the electrical performance of TWCNTs are similar to that of SWCNTs because of the reduced diameter of the walls (i.e., enhanced electrical conductivity). Despite the advantages of TWCNTs over other types of CNTs, investigations into TWCNT-embedded cementitious materials are insufficient.

Several studies have attempted to investigate the physicochemical and electrical properties of CNT-embedded UHPC to simultaneously secure the inherent characteristics of CNTs and UHPC (i.e., electrical conductivity and superior mechanical properties) [16,18,26–28]. However, the combinations of TWCNTs and UHPC have not yet been showcased and are considered a challenge in the relevant fields. Motivated by the fact that the electrical performances of TWCNT are similar and superior to those of SWCNT and MWCNT, respectively, the incorporation of TWCNT into UHPC is anticipated to be beneficial from the engineering viewpoint. Nevertheless, the possible microstructural alteration induced by the use of TWCNT remains unveiled fully thus far. In particular, the characterization of TWCNT-embedded UHPC is essential because the fresh and hardened properties of UHPC have been revealed to be vastly modified by CNT incorporation. Therefore, the present study aims to provide comprehensive works including material characterization and piezoresistive sensing capabilities.

This study characterized TWCNT-embedded UHPC and evaluated its piezoresistive sensing capabilities. Material characterization of the fresh and hardened TWCNT-embedded UHPC samples was performed using a table flow test, initial and final setting time measurements, isothermal calorimetry, autogenous shrinkage measurements, X-ray diffractometry (XRD), solid-state ^{29}Si magic angle spinning nuclear magnetic resonance (MAS NMR), scanning electron microscopy (SEM), compressive and flexural strength tests, and mercury intrusion porosimetry (MIP). The electrical and piezoresistive sensing properties of the samples were assessed by electrical resistivity measurements and fractional change in resistance (FCR) calculations upon 5000 cycles of dynamic compressive loading tests. The present study will be a cornerstone in the fundamental understanding of TWCNT-embedded UHPC, broadening insights into relevant industries and stakeholders.

2. Sample preparation and testing details

2.1. Sample preparation and casting/curing procedures

Type I ordinary Portland cement and silica fume were used as binder materials. Silica powder was added to the samples as an inert filler. Sand with a particle size in the range of 0.17–0.7 mm was included as the aggregate. Sand was excluded during the preparation of the paste samples. A polycarboxylate-based superplasticizer (SP) was used to achieve a water-to-cement ratio of 0.23 in the samples. TWCNTs were additionally added to cement at levels from 0 to 0.5% by the mass of cement. TWCNTs produced by JEIO Co., Ltd., South Korea, were used. Mix proportion of the samples is shown in Table 1.

The cement, silica fume, silica powder, sand, and TWCNTs were mixed for 15 min to ensure the proper and homogenous mixing state of TWCNTs using the Hobart pan mixer, followed by 10 min of wet mixing. Note that TWCNTs were mechanically mixed with powders without being treated with the ultra-sonication. The fresh slurry was cast into designated molds and underwent 1 d of initial curing at 25 °C, and its surface was sealed with plastic tape to prevent the natural evaporation of water or carbonation. After 1 d of initial curing, the hardened samples were demolded and steam-cured for additional 3 d. The temperature was maintained at 90 °C throughout the steam curing period. The samples were then sealed in plastic bags and cured in a curing chamber controlled at 25 °C. The UHPC samples were used for table flow tests, initial and final setting time measurements, autogenous shrinkage measurements, compressive strength, electrical resistance, and piezoresistive sensing capability assessments, while paste samples were used for XRD, SEM, isothermal calorimetry, and solid-state ^{29}Si NMR spectroscopy. UHPC samples with dimensions of 50 × 50 × 50 mm were used for the compressive strength, electrical resistance, and piezoresistive sensing capabilities. The samples for isothermal calorimetry and autogenous shrinkage measurements were not treated with the steam curing process.

Table 1
Mixture proportion of the samples expressed as weight ratio.

Cement	Silica fume	Silica powder	Sand (excluded for paste samples)	Super-plasticizer	Water	TWCNT
100	25	35	110	4	23	0 0.1 0.2 0.3 0.5

2.2. Test methods

The XRD patterns of the raw materials and hardened samples were acquired from the Korea Basic Science Institute (KBSI) Daegu Center. XRD was performed under a CuKα generator voltage and tube current of 40 kV and 30 mA, respectively. The scanned Cu-Kα range was 5 °–65° 2θ (°). The SEM images of the samples were obtained using a high-resolution SEM device manufactured by Hitachi (S-4800). Bulk samples with diameters of less than 3 mm were used for SEM analysis. The raw materials were blown onto the carbon tape attached to the sample puck. The samples were pretreated with Pt using a Pt ion beam sputter-coating device to impart conductivity to the samples. The surfaces of the coated samples were then explored using an SEM device under a vacuum. The table flow tests of the fresh-state samples were performed using the testing provision outlined in ASTM C1437-20 [29]. The initial and final setting times were identified by following the test protocols provided in ASTM C191-08 [30]. Isothermal calorimetry measurements of the samples were performed using a three-point multipurpose conduction calorimeter (Tokyo-Riko Co., Ltd.). The isothermal heat release rate of the samples was measured for 72 h. The autogenous shrinkage of the samples was measured using a paddle-type gauge embedded at the center of the prismatic mold (40 × 40 × 40 mm) before casting. Autogenous shrinkage was monitored after final setting of the samples [31]. At the final setting, the samples were carefully demolded and sealed with plastic wrap to prevent drying shrinkage owing to the evaporation of internal moisture. The sealed samples were placed in a curing chamber at 25 °C. The bottom surface of the chamber was treated with oil to minimize friction between the samples and chamber surface. The embedded gauges were connected to a data logger in order to convert electrical signals into digits. The reading interval was fixed at 10 min. The autogenous shrinkage was measured for 165 h after the final setting. The solid-state ^{29}Si MAS NMR spectra of the samples were obtained at 79.5 MHz at a spinning rate of 11.0 kHz, pulse length of 1.6 μsec, and relaxation delay of 20 s. External tetrakis(trimethylsilyl)silane

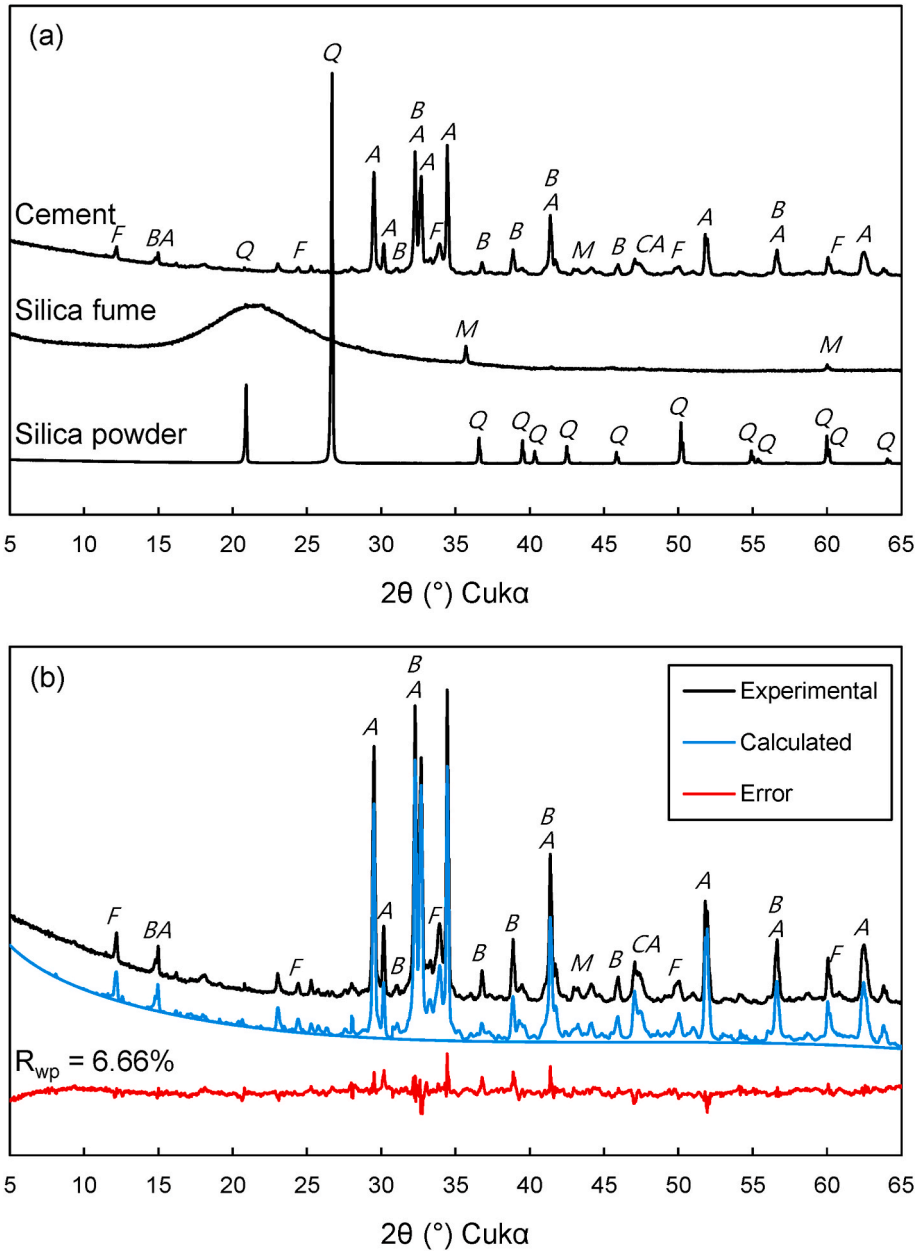

Fig. 1. X-ray diffractograms of (a) raw materials and (b) Rietveld analysis result of raw cement. The annotations indicate the following: F—brownmillerite, BA—basanite, A—alite, B—belite, M—periclase, CA—calcium aluminate, and Q—quartz.

was used to calibrate the chemical shift at 0 ppm. The compressive strength of the samples was measured using a 1000 kN compressor. The loading rate was manually controlled at 0.2 MPa/s. MIP was carried out using an AutoPore IV 9500 device manufactured by Micromeritics Instrument Corporation. The maximum mercury intrusion pressure was 420.6 MPa. Bulk fractions of samples with diameters less than 3 mm were used for the MIP analysis. The DC electrical resistances of the samples were measured using a portable digital multimeter (Keysight U1282A), and the measured resistances were converted to electrical resistivity considering the sizes of the electrodes with a 50 mm length and 20 mm width. The piezoresistive sensing capabilities were investigated under the dynamic compressive loading tests. As reported in the previous studies [25,32,33], the electrical characteristics and piezoresistive sensing capabilities are known to be affected by the residual moisture in the cementitious composites. To remove any uncertainties raised by the residual moisture content present in the samples, the samples for these analyses were exposed 50 °C for 3 d to evaporate the residual moisture. Dynamic loading with 30 MPa of triangular loading and a frequency of 0.5 Hz was applied to the samples, and their electrical resistances were measured simultaneously using a digital multi-meter (Agilent Tech, 34410A). The FCR was then calculated considering the initial electrical resistance of the samples. Loadings with various frequencies (0.5, 1.0, 2.0, and 4.0 Hz) were applied to the samples to understand the effects of the loading frequencies on the sensing capabilities of the samples, and their FCR values were measured as described above. Finally, the long-term sensing capabilities of the samples were investigated under 5000 cycles of compressive loading.

2.3. Properties of raw materials

The XRD patterns of cement, silica fume, and silica powder are shown in Fig. 1 (a). Unlike cement and silica powder, silica fume primarily exhibited a broad hump with minor traces of periclase. Rietveld analysis of the XRD pattern of the cement was performed as shown in Fig. 1 (b), and the results are summarized in Table 2 along with the X-ray fluorescence data of the cement, silica fume, and silica powder (provided by the manufacturer). The diameter and length of the corresponding TWCNTs used in this study were 4–9 nm and 10–200 μm, respectively. The purity of the TWCNTs were higher than 98.5 wt% and their specific surface area was about 400–700 m^2/g.

Table 2
Chemical and mineral compositions of the binder materials used in this study.

X-ray fluorescence (wt%)				Rietveld calculation (wt%)	
	Cement	Silica fume	Silica powder		Cement
SiO_2	20.4	96.8	99.1	C_3S	56.2
Al_2O_3	4.6	0.1	0.15	C_2S	12.3
CaO	60.3	0.1	–	C_4AF	11.3
Fe_2O_3	3.2	0.8	–	C_3A	8.0
MgO	3.3	0.2	–	$C\overline{C}$	4.4
TiO_2	0.3	–	0.11	C$·0.5H	3.3
SO_3	2.3	–	–	CH	1.9
Mn_2O_3	0.1	–	–	C$·2H	1.1
P_2O_5	0.1	–	–	C	0.8
SrO	0.1	–	–	M	0.7
Na_2O	0.2	0.1	–	C$	0.1
K_2O	0.9	0.4	–		
ZrO_2	–	–	–		
LOI[a]	4.5	1.5	0.62		

[a] Loss-on-ignition.

3. Characterization of TWCNT-embedded UHPC

3.1. Fresh-state behavior

The table flow level of the samples is provided in Fig. 2. The table flow values tended to decrease as the TWCNT content increased. The table flow value of the sample without TWCNTs was measured as 170 mm and rapidly reduced upon incorporation of TWCNTs, reaching a table flow value of 103 mm for the sample with TWCNT content of 0.5%, which was 39% lower than that of the table flow value of the sample without TWCNTs. The reduction in the table flow induced by the incorporation of TWCNTs can be explained either by the large specific surface area or by the water absorption property of TWCNTs [27]. In particular, the large specific surface area of TWCNTs triggered the attraction between cement particles, which significantly increased the plastic viscosity of the fresh-state samples and contributed to a reduction in the table flow values [34]. Meanwhile, the appropriate dispersion of TWCNTs in the presence of polycarboxylate-based SP occurred via interactions between TWCNTs and the nonpolar groups of SP [35]. Nevertheless, the efficiency of using such a SP was known to be sharply degraded upon blending more than a certain amount of TWCNTs because of the formation of excessive TWCNT agglomerates in the matrix, as clearly tackled by earlier work [36]. This phenomenon was likely reflected in Fig. 2 to some extent. In this context, the sample without TWCNTs showed self-compacting properties during casting, while a proper rod-tamping process was necessary for the samples with TWCNTs. Note that the active tamping action was performed by tamping the surface of the poured fresh-state mixture every one-sixth of the height of mold reached. This process was iterated six times for a single sample preparation regardless of the sample dimension. Despite the fact that active tamping was applied to the samples with TWCNTs, the electrical properties of the samples (as illustrated in the later Sections) with various TWCNT contents were fairly distinguishable, which would otherwise be impossible if TWCNT agglomeration was a critical problem during casting.

The initial and final setting times of the samples are shown in Fig. 3. The addition of TWCNTs clearly led to the decrease in both the initial and final setting times of the samples. The sample with TWCNT content of 0.1% displayed similar initial and final setting times to the sample without TWCNTs, yet the incorporation of TWCNTs at 0.3% and 0.5% significantly reduced the initial and final setting times of the samples. This was likely due to the interaction between cement particles and TWCNTs, which accompanied the increased viscosity of the fresh-state

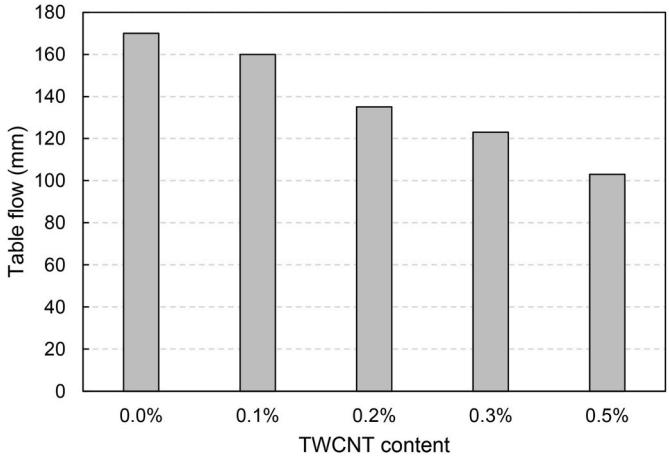

Fig. 2. Table flow level of the samples.

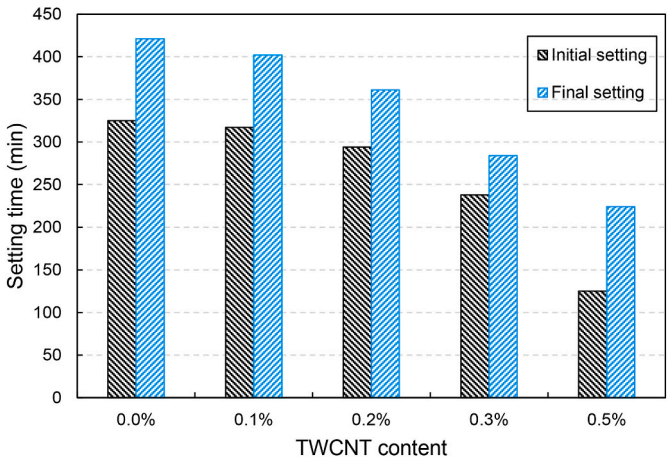

Fig. 3. Initial and final setting times of the samples.

paste and negatively affecting the workability [37,38]. From the viewpoint of hydration, the incorporated TWCNT induced a nucleation effect in the initial hydration of C_3A, thus advancing the hydration kinetics [39]. The occurrence of this nucleation effect was closely related to the polarization and adsorption between the cement particles and nano-sized TWCNTs [40]. The stiffening and setting properties of fresh-state cement paste were heavily dependent on the hydration rate of aluminate clinkers (mainly C_3A in cement) [37,41]. However, the appearance of a rapid nucleation effect adversely affected hydration at a later stage, hindering the additional hydration of the clinkers [39]. Therefore, in the presence of TWCNTs exceeding a certain threshold, the rapid formation of nuclei resulted in the rapid growth of hydrates, which ultimately induced a barrier effect on the hydration of clinkers [42]. The initial and final setting times of the sample with TWCNT content of 0.5% were 125 min and 224 min, respectively, each representing 62% and 47% reduced values of the initial and final setting times of the sample without TWCNTs, respectively.

3.2. Hydration kinetics and products

The cumulative heat release and heat release rate of the samples are shown in Fig. 4. During the initial 10 h of hydration, no significant differences in the cumulative heat release of the samples with various TWCNT content were observed. However, the sample with TWCNT content of 0.2% showed the highest cumulative heat afterward, followed

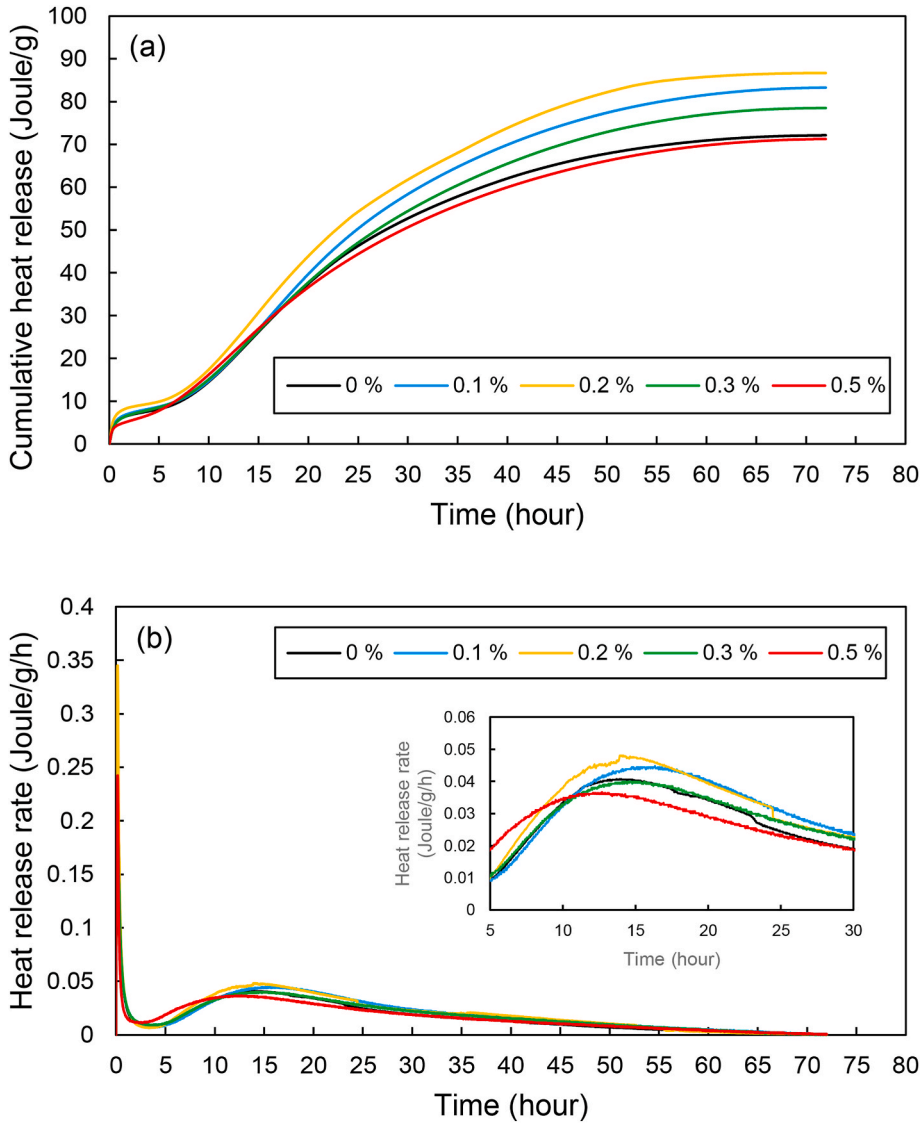

Fig. 4. (a) Cumulative heat release and (b) heat release rate of the samples during the initial 72 h of hydration.

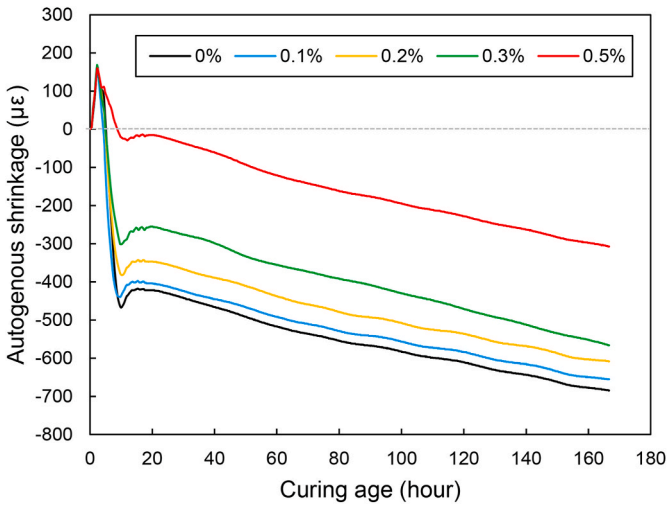

Fig. 5. Autogenous shrinkage development of the samples for 165 h after final setting.

by the samples with TWCNT contents of 0.1% and 0.3%. On the contrary, the sample with TWCNT content of 0.5% exhibited less cumulative heat release than that of the sample without TWCNTs. The cumulative heat release levels of the samples with TWCNT contents of 0, 0.1, 0.2, 0.3, and 0.5% recorded at the end of the measurement were 72.14, 83.26, 86.67, 78.49, and 71.28 J/g, respectively. Fig. 4 (b) displays the heat release rate of the samples and the typical heat release aspects that occur upon cement hydration. The first symptom was found approximately at the commencement of measurement, which was an exothermic peak owing to the rapid dissolution of cement grains during contact with water, coupled with the hydration phenomenon in which Ca^{2+} and SO_4^{2-} ions present in the solution react with C_3A to form ettringite [42]. The induction period and acceleration/deceleration events (typically referred to as the main peak) were generated after the occurrence of the first peak. The main peak primarily indicated the hydration of C_3S, with this peak preceded by the precipitation of C–S–H and portlandite, followed by the depletion of sulfate [43,44]. In the induction and main peak periods, the samples exhibited varying features with different TWCNT contents. The induction periods of the samples with TWCNTs were slightly shorter than those of the sample without TWCNTs. This outcome was possibly attributed to the nucleation effect induced by the addition of TWCNTs, which advanced the occurrence of the main exothermic reaction [40,43]. In contrast, opposite results were reported in earlier studies [45,46], demonstrating that the addition of TWCNTs prolonged the induction period, probably due to surfactant adsorption on the cement grains. However, this phenomenon did not permanently persist and resume after a certain curing period, showing an increased total heat release at the end of the measurement [45], an outcome analogous to that in this study. The intensity of the main peak of the heat release rate of the sample with TWCNT content of 0.5% was observed to be lower and blunted as compared with that of other samples. The excessive incorporation of TWCNTs hindered the hydration of cement by covering the clinkers, acting as a barrier in the growth of hydrates [47]. The hydration of cement in the presence of TWCNTs benefited from the occurrence of the nucleation effect and, at the same time, was inhibited if the TWCNT dosage was excessive. It was estimated that the TWCNT content corresponding to the threshold point of this phenomenon was between 0.3 and 0.5%. The deceleration period manifested the transformation of ettringite into monosulfate [44] and did not show differences with varying TWCNT contents because TWCNT incorporation did not correlate with the total amount of ettringite.

The autogenous shrinkage development of the samples for 165 h after final setting is shown in Fig. 5. The measurement was initiated by showing an expansion for all samples. The expansion phenomenon observed in the very early stage was associated with the hydration of the free lime present in the cement [48,49]. The hydration of free lime accompanied the volumetric increase of approximately 2.5 times by forming $Ca(OH)_2$ which created pores in the matrix and induced an increase in the total volume [48,50,51]. The incorporation of TWCNTs did not affect the hydration kinetics of the free lime, given that the rate and amount of expansion observed in the samples were almost identical regardless of the TWCNT content. Subsequently, rapid autogenous shrinkage development was observed in all samples until 12 h. This rapid shrinkage was generally found in the samples with an extremely low water-to-binder ratio, which is very vulnerable to self-desiccation, consequently leading to high autogenous shrinkage [52]. Therefore, the UHPC samples prepared in this study typically exhibited rapid and intense autogenous shrinkage development. The measured time of the occurrence of rapid autogenous shrinkage was approximately identical to the symptoms observed at 12–15 h in the isothermal calorimetry test results, considering the setting time. Thus, rapid shrinkage occurred as the active hydration of C_3S began during this period. The degree of the autogenous shrinkage in the samples decreased proportionally as the TWCNT content increased. From the isothermal calorimetry test results, a higher exothermic peak was noted for the samples with TWCNT content of 0.1 and 0.2% in this period, however the autogenous shrinkage development followed changes proportional to TWCNT contents, regardless of heat release rate results. It was likely that the nano-reinforcing effect of TWCNTs occurred because the incorporation of TWCNTs promotes hydration, while physically interconnecting the hydration products formed at an early age [53]. In addition, hydration products placed in-between TWCNT bundles can reinforce and stiffen the matrix, which in turn limited the development of autogenous shrinkage [53]. On the one hand, the sample with TWCNT content of 0.5% showed the least amount of autogenous shrinkage in this period, as the excessive incorporation of TWCNTs possibly interfered with hydration, prevailing the overall kinetics.

The XRD patterns of the samples are shown in Fig. 6. The mineralogical compositions of the samples contained C_3S (PDF# 00-042-0551), C_2S (PDF# 00-033-0302), and C_4AF (PDF# 00-011-0124), all of which originated from raw cement. In addition, peaks corresponding to quartz (PDF# 00-046-1045) were marked on the patterns owing to the presence of silica powder. The samples showed no significant differences in the phase composition and peak intensities between 7 and 28 d of curing, as the samples underwent steam temperature curing before 7 d of curing, indicating that the samples had already reached a sufficient hydration degree at 7 days of curing. The absence of hydration products, such as ettringite, was identified because this product was thermally decomposed during curing [54]. Furthermore, portlandite was fully consumed by the pozzolanic reaction with silica fume to form C–S–H [55,56]. The addition of TWCNTs did not result in a noticeable change in the patterns.

The solid-state ^{29}Si NMR spectra of anhydrous samples are shown in Fig. 7. The spectrum of the raw cement resonated with a sharp feature centered at approximately −71 ppm (Q^0 site), which combines broad and narrow resonances from C_3S and C_2S, respectively [57]. Silica fume and silica powder resonated in the Q^4 region, each centered at approximately −108 and −107 ppm, respectively. The solid-state ^{29}Si NMR spectra of the samples at 28 d of curing are shown in Fig. 8. Resonance of the unhydrated fraction (Q^0 site), silica fume, and silica powder were commonly observed in the samples. The microstructure of the C–S–H in the hydrated samples was clearly revealed by the spectra. The resonance

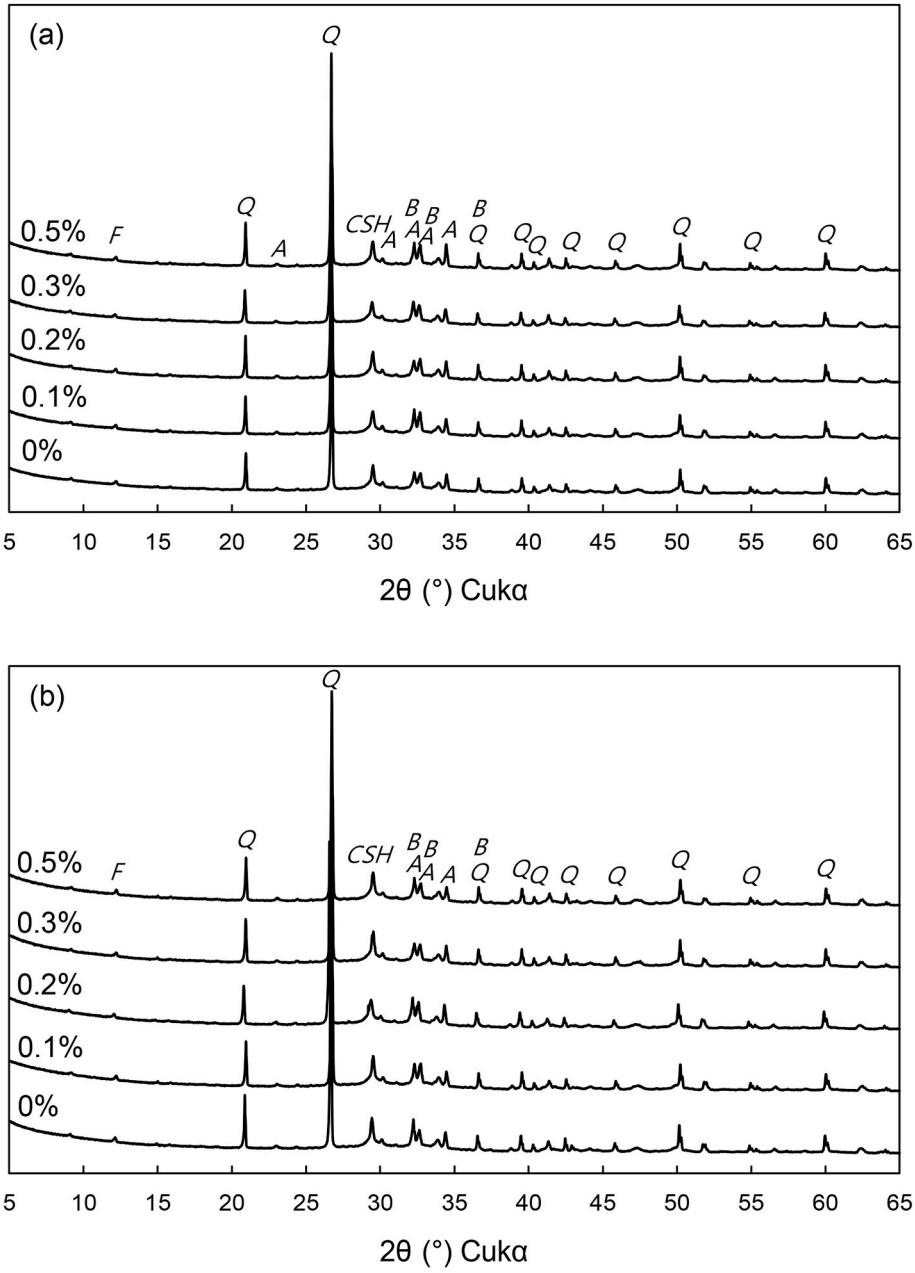

Fig. 6. X-ray diffractograms of the samples at (a) 7 and (b) 28 d of curing. The annotations indicate the following: F—brownmillerite, Q—quartz, A—alite, B—belite, and CSH—calcium silicate hydrate.

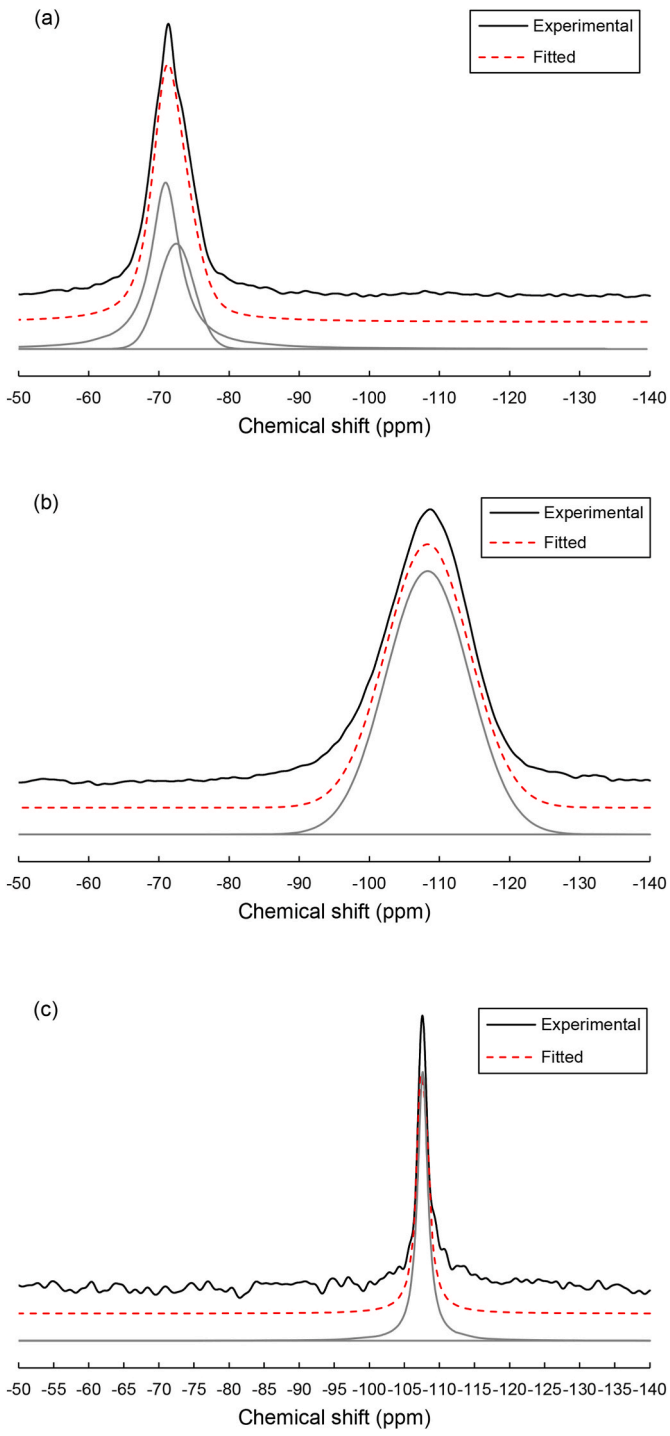

Fig. 7. Solid-state ^{29}Si NMR spectra of (a) raw cement, (b) silica fume, and (c) silica powder.

at −79, −83, and −85 ppm was assigned to the end (Q^1), bridging (Q^2b), and paired (Q^2p) Si members in the C–S–H chain, respectively [58,59]. Al substitution in the Si chains of C–S–H was also indicated by the resonance at −81 ppm which corresponds to the Q^2(1Al) site, a bridging Al atoms substituted for Si in the bridged site of C–S–H [60]. In addition, the presence of highly cross-linked Si was indicated by Q^3(1Al) and Q^3 sites, which were the result of the steam curing process [61]. Deconvolution of the spectra was performed to quantitatively analyze the Si fractions of the sites. Deconvolution was performed based on the simulated raw materials, as shown in Fig. 7. The deconvolution calculation was iterated to reach an estimated chi-square value of 10^{-6}. The relative Si fractions of the samples, as calculated from the deconvolution of ^{29}Si NMR spectra, are shown in Fig. 9. The Q^0 fraction decreased as the CNT content increased and started to increase when the TWCNT content was higher than 0.2%. The Q^0 fraction is regarded as a quantitative index that represents the degree of silicate clinkers hydration in cement. Thus, hydration was promoted with the aid of TWCNT-induced nucleation effect until the TWCNT content was 0.2%. However, the incorporation of TWCNT content exceeding 0.2% hindered hydration despite that the samples underwent the steam curing process. Meanwhile, the summation of Q^1, Q^2(1Al), Q^2b, and Q^2p fractions, which can be evaluated as the total amount of C-(A)-S-H, were 43.5, 44.9, 42.2, 44.5, and 40.5% in the samples with TWCNT contents of 0, 0.1, 0.2, 0.3, and 0.5%, respectively, which did not differ significantly except for the sample with TWCNT content of 0.5%. However, the structural features of the formed C-(A)-S-H clearly indicated that an increase in the TWCNT content increased the degree of Al substitution. Furthermore, the samples with TWCNT content of 0.1 and 0.2% showed increased Q^3(1Al) and Q^3 fractions as compared to those with the sample without TWCNTs. This meant that the incorporated TWCNT led to the partial substitution of the interlayer of C-(A)-S-H with highly cross-linked Si bridged with Al. A similar test result was reported in earlier work [18,62,63] which explained that the Si chain of C-(A)-S-H formed around the TWCNT was influenced by the geometry of the TWCNT. The mean chain length (MCL) of C-(A)-S-H, calculated using Eq. (1) [64], was 14.92, 17.47, 22.53, 20.15, and 20.90 for the samples with TWCNT contents of 0, 0.1, 0.2, 0.3, and 0.5%, respectively.

$$\mathrm{MCL} = 4[Q^1 + Q^2 + Q^2(1\mathrm{Al}) + Q^3 + 2Q^3(1\mathrm{Al})]/Q^1 \text{ [64].} \qquad \text{Eq.(1)}$$

The silica fume fraction showed no particular trend or differences according to the TWCNT content, indicating that the TWCNT did not affect the extent of the pozzolanic reaction of the silica fume. The silica powder fraction was regarded as inert and did not participate in the reaction.

The SEM images of the samples containing TWCNTs are shown in Fig. 10. TWCNTs were observed in the samples and became clearer as the TWCNT content increased. TWCNTs were found to be anchored throughout the hydration products, which was visually interpreted as the occurrence of a nano-reinforcing effect. Furthermore, the growth of hydration products at the perimeter of the CNT was also indicated in the SEM images. The sample with TWCNT content of 0.5% particularly showed the presence of bundles of TWCNTs, indicating the formation of dense conductive networks in the matrix.

3.3. Physical properties

The compressive and flexural strengths of the samples are shown in Fig. 11. The compressive strength of the samples was not enhanced between 7 and 28 d of curing because a sufficient hydration degree was reached during the steam curing process. The compressive strength did not vary according to TWCNT contents, yet the samples with TWCNT contents of 0.3 and 0.5% were slightly reduced as compared to the sample without TWCNTs. The rates of change in the compressive strength of the samples with TWCNT contents of 0.1, 0.2, 0.3, and 0.5% with respect to the sample without TWCNTs were −5.47, 1.05, −7.38, and −5.52% at 7 d of curing, respectively, and −2.55, 0.53, −5.17, and −5.64% at 28 d of curing, respectively. Contrary to the compressive strength results, the flexural strength showed a notable difference with different TWCNT content. The incorporation of TWCNT content equal to or greater than 0.3% caused a deteriorating effect on the flexural

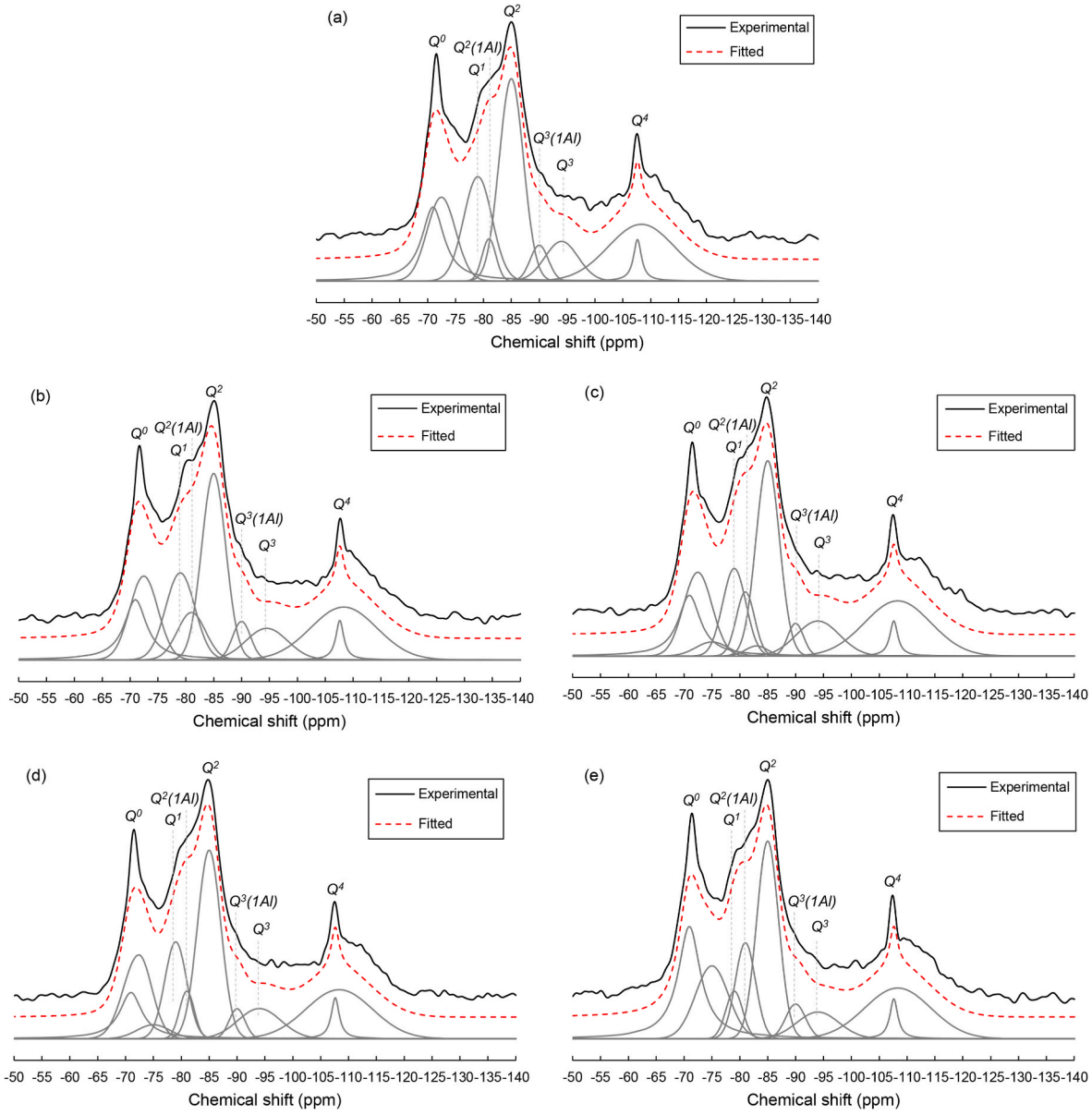

Fig. 8. Solid-state ^{29}Si NMR spectra of the samples with TWCNT content of (a) 0%, (b) 0.1%, (c) 0.2%, (d) 0.3%, and (e) 0.5%.

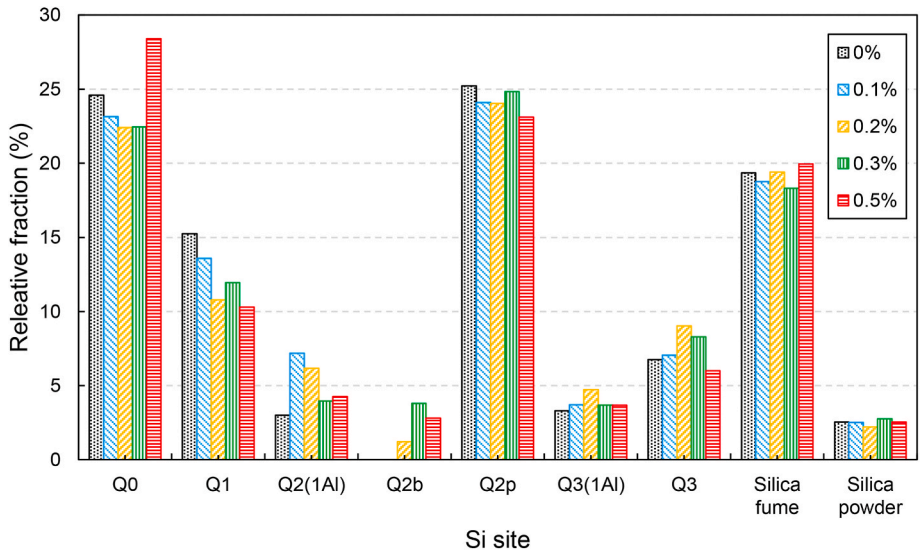

Fig. 9. Relative Si fraction (%) of the samples as calculated from the deconvolution of ^{29}Si NMR spectra.

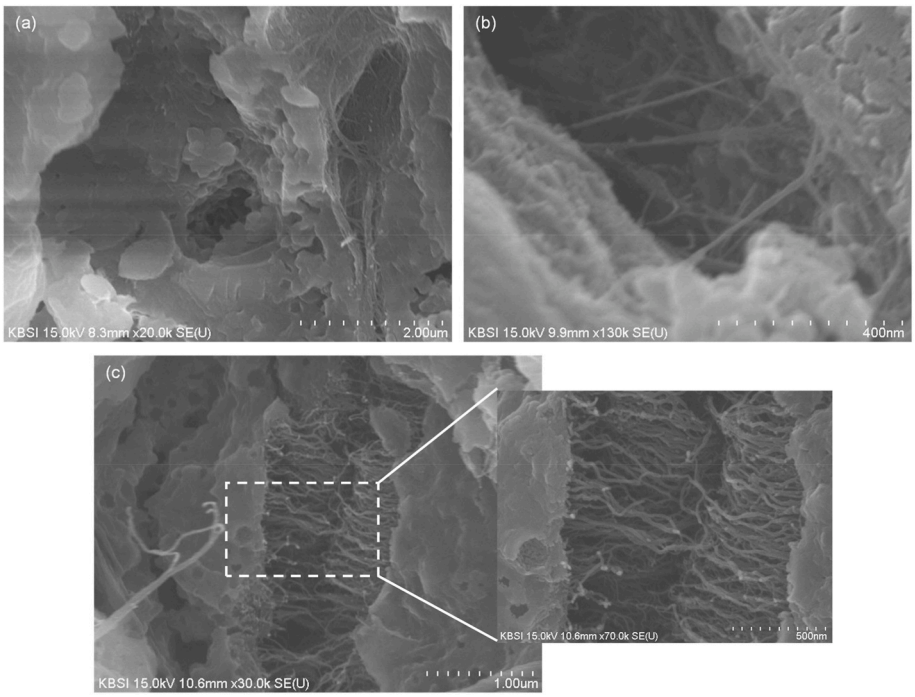

Fig. 10. Scanning electron microscopy images of the samples with TWCNT content of (a) 0.2%, (b) 0.3%, and (c) 0.5%.

strength at 7 d of curing. The flexural strength of the sample without TWCNTs at 28 d of curing was almost identical to that measured at 7 d of curing, while the samples with TWCNTs displayed enhancements in the flexural strength between 7 and 28 d of curing, all of which showed a higher flexural strength than the sample without TWCNTs. The rates of change in the flexural strength of the samples with TWCNT contents of 0.1, 0.2, 0.3, and 0.5% with respect to the sample without TWCNTs were 18.64, 13.88, 5.40, and 1.08% at 28 d of curing, respectively, showing a decreasing trend with an increase in TWCNT content. Overall, based on the compressive and flexural strength values of the samples at 28 d of curing, no serious strength degradation occurred upon incorporation of TWCNTs, meaning that the TWCNT contents used in this study can secure sufficient mechanical strength development. Numerous earlier works demonstrated the alterations in the mechanical strength of cement-based composites by the incorporation of CNT [16–19,65,66]. However, the mechanical strength levels of the samples at 28 d of curing provided in this study were scarcely changed by the TWCNT contents, meaning that the mechanical strength development of the TWCNT-embedded UHPC was governed by the steam curing process rather by the TWCNT content.

The cumulative pore volume and logarithmic derivative of the samples at 28 d of curing are shown in Fig. 12. The cumulative pore volume of the samples tended to increase as the TWCNT content increased, but the maximum cumulative intrusion was reached for the sample with TWCNT content of 0.3%. As shown in Fig. 12 (b), all samples mainly contained pores with diameters less than 10 nm, which were closely associated with the presence of C-(A)-S-H gel pores formed by the hydration of clinkers and pozzolanic reaction [67]. Other than

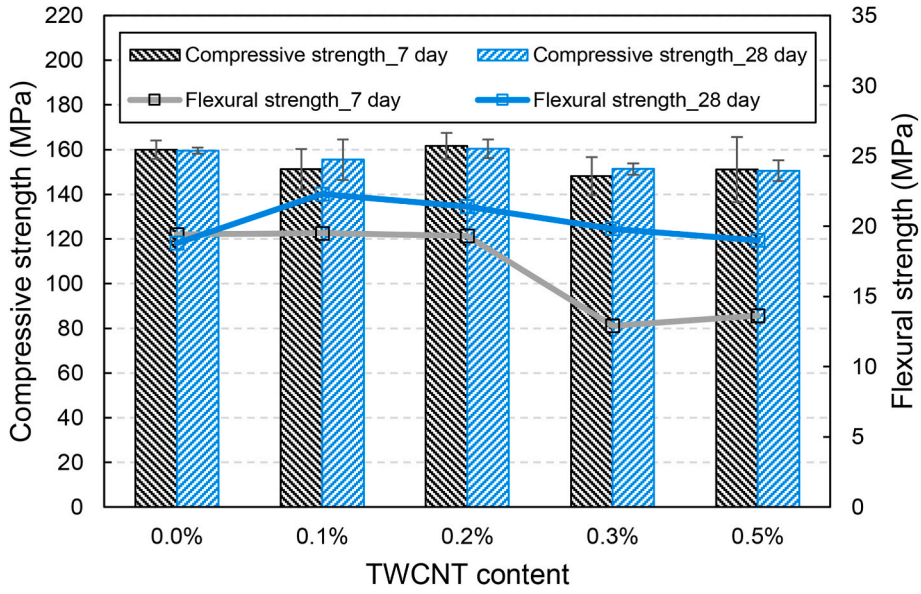

Fig. 11. Compressive and flexural strengths of the samples.

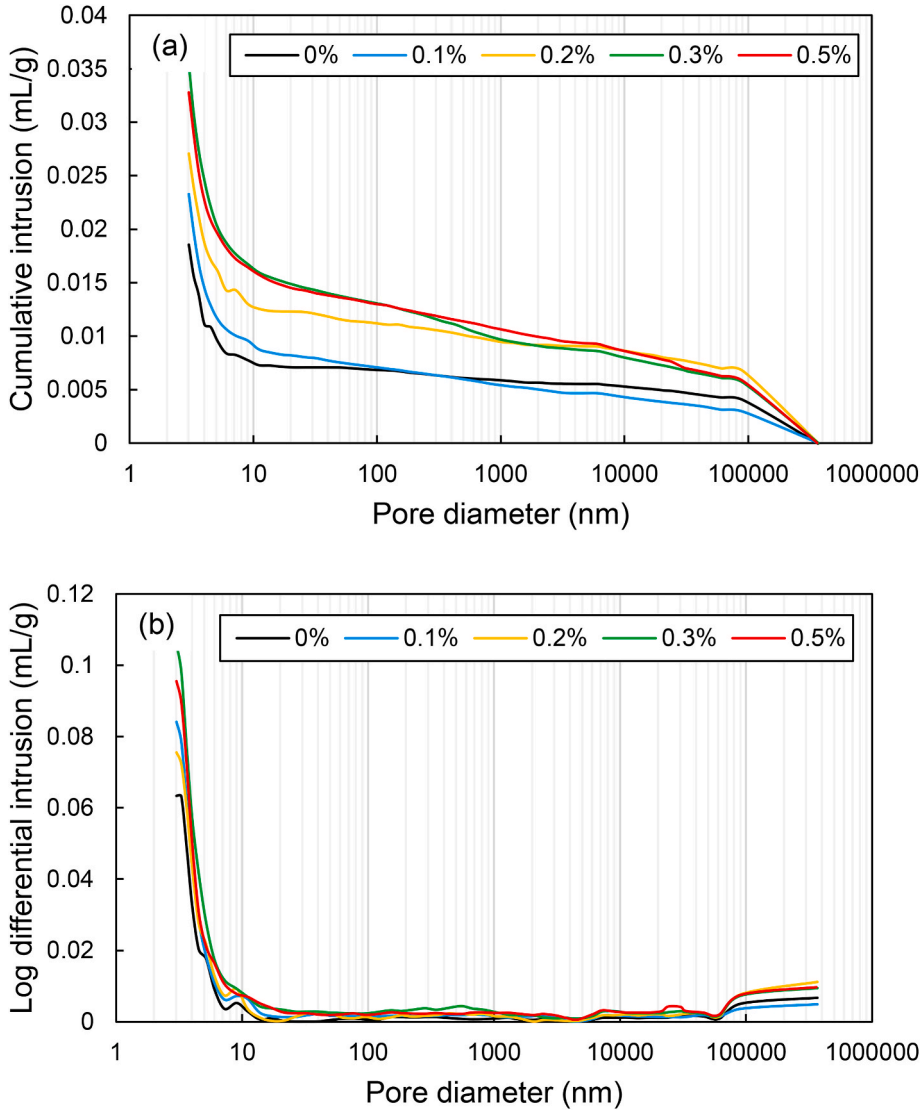

Fig. 12. (a) Cumulative pore volume and (b) logarithmic derivative of the samples at 28 d of curing.

this pore diameter range, no noticeable pore population was observed. The porosity and total pore area of the samples at 28 d of curing are shown in Fig. 13. The porosity and total pore area of the samples followed the same trend. The porosity was the lowest in the sample without TWCNTs (4.00%) and the highest in the sample with TWCNT content of 0.3% (7.45%). The porosity of the sample with TWCNT content of 0.5% was rather slightly lowered to 6.97%. It was provided in Jung et al. [17] that the volume corresponding to the entrained and entrapped air voids increased as the CNT content increased. Similarly, the pore volume having diameters of 500–1000000 nm was increased upon TWCNT incorporation, which may have brought in the differences in the porosity levels in the samples. However, as proven in Fig. 11, the strength of the samples at 28 d of curing was all similar, meaning that the strength development was more influenced by the improved reaction degree of binders due to steam curing than by the TWCNT content.

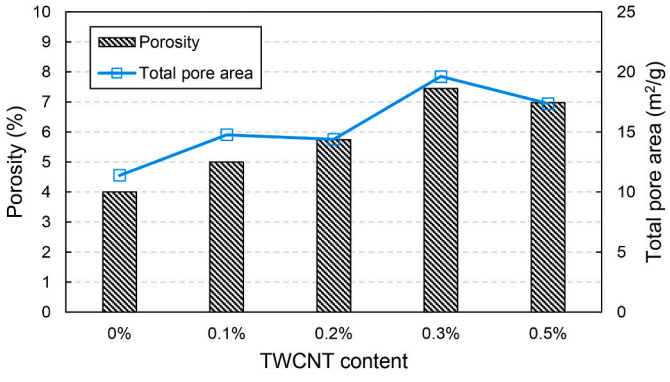

Fig. 13. Porosity and total pore area of the samples at 28 d of curing.

4. Piezoresistive sensing capability

The electrical resistivity values of the samples are shown in Fig. 14. The measured electrical resistance was converted into electrical resistivity considering the area of the electrodes (10 cm^2) and the distance between the two electrodes (2 cm). The electrical resistivity decreased as the TWCNT content increased. However, the degree of decrease in electrical resistivity differed according to the embedded TWCNT content. A dramatic decrease in the electrical resistivity was found for the TWCNT contents of 0–0.2%. After this point, the extent of the decrease in electrical resistivity decreased. This range was referred to as the percolation threshold, where conductive networks consisting of TWCNTs were developed, thereby increasing the electrical conductivity [20]. The obtained percolation threshold range (i.e., 0.1–0.2%) was

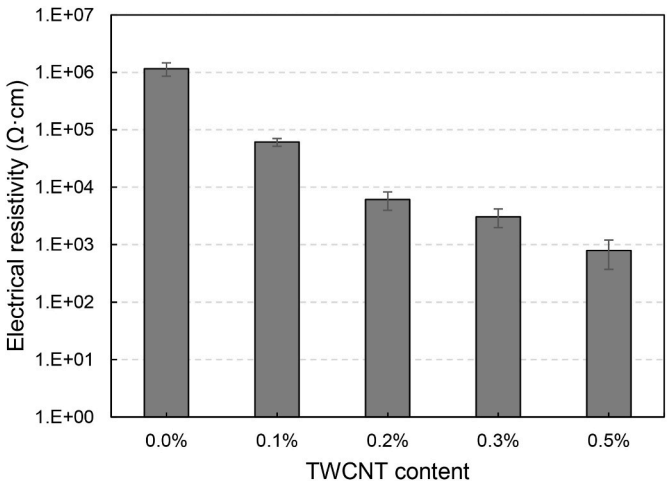

Fig. 14. Electrical resistivity values of samples.

equal to or lower than those found in the previous studies [24,68], indicating that the TWCNTs were well dispersed in the cementitious composites.

The samples were loaded for 5 cycles and their piezoresistive sensing performances under cyclic loading are shown in Fig. 15. The sample with TWCNT content of 0.2% exhibited the highest value of FCR among the samples with TWCNTs. This result was deduced from the piezoresistive sensing mechanisms and percolation threshold. The piezoresistive sensing mechanism indicated the relationship between applied load and electrical conductivity [15]. Upon loading, the distances between the adjacent embedded TWCNT particles decreased, which can increase the electrical conductivity. In contrast, the TWCNT particles tended to return to their original position and hence, the distances between adjacent TWCNT particles increased as the loading decreased. When a high amount of TWCNTs were embedded in the composites, they could form dense conductive networks, causing smaller movements of TWCNT particles and lower electrical conductivity changes. However, the electrical conductivity change increased with the TWCNT content in the percolation threshold because the small movements of TWCNT particles lead to a higher change in electrical conductivity based on the definition of the percolation threshold [24]. In addition, the obtained FCR value (i.e., 65%) in samples with TWCNT content of 0.2% under the 30 MPa was much higher than that found in the previous studies [69–71]. Typically, low levels of loading were chosen for application to the composites in previous studies because the compressive strength of the samples used in their work was much lower than those used in this study. Thus, the high compressive strength of the samples used in this study enabled the use of high compressive loadings, leading to a higher FCR and ensuring high sensitivity of the cement-based sensors.

The FCR of the samples under monotonic compressive loading at various loading frequencies is shown in Fig. 16. The stability of FCR was significantly affected by the TWCNT content. The samples with TWCNT content of 0.1% showed different levels of FCR values at different loading frequencies. However, this phenomenon decreased as the TWCNT content increased. As a small amount of TWCNTs were added to the composites, the disturbances of TWCNT-based conductive networks which cause changes in electrical conductivity were more dominant than those of composites with large amounts of TWCNTs. This was because the content of conductive filler in the sample with TWCNT content of 0.1% was relatively lower than that of other samples which

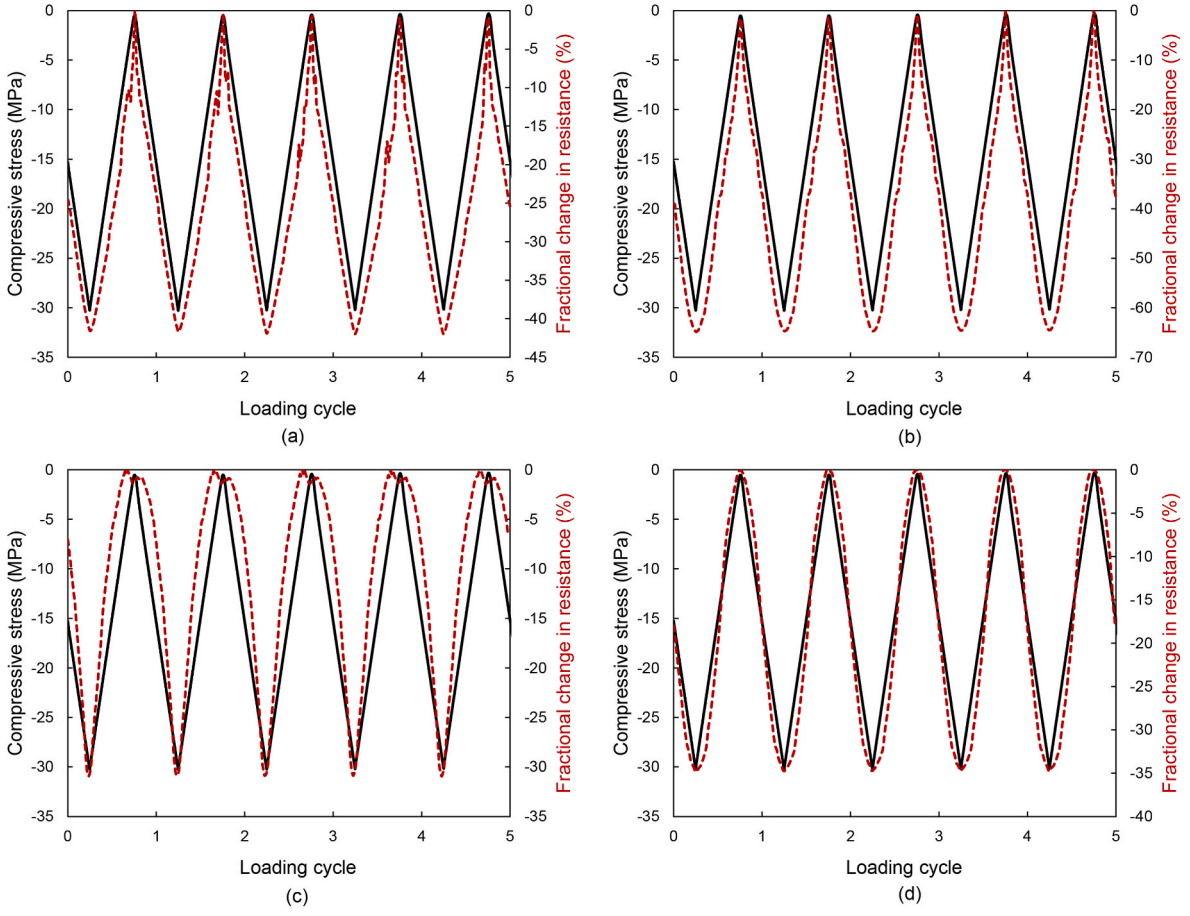

Fig. 15. Piezoresistive sensing performances of samples with TWCNT content of (a) 0.1, (b) 0.2, (c) 0.3, and (d) 0.5% under cyclic loadings.

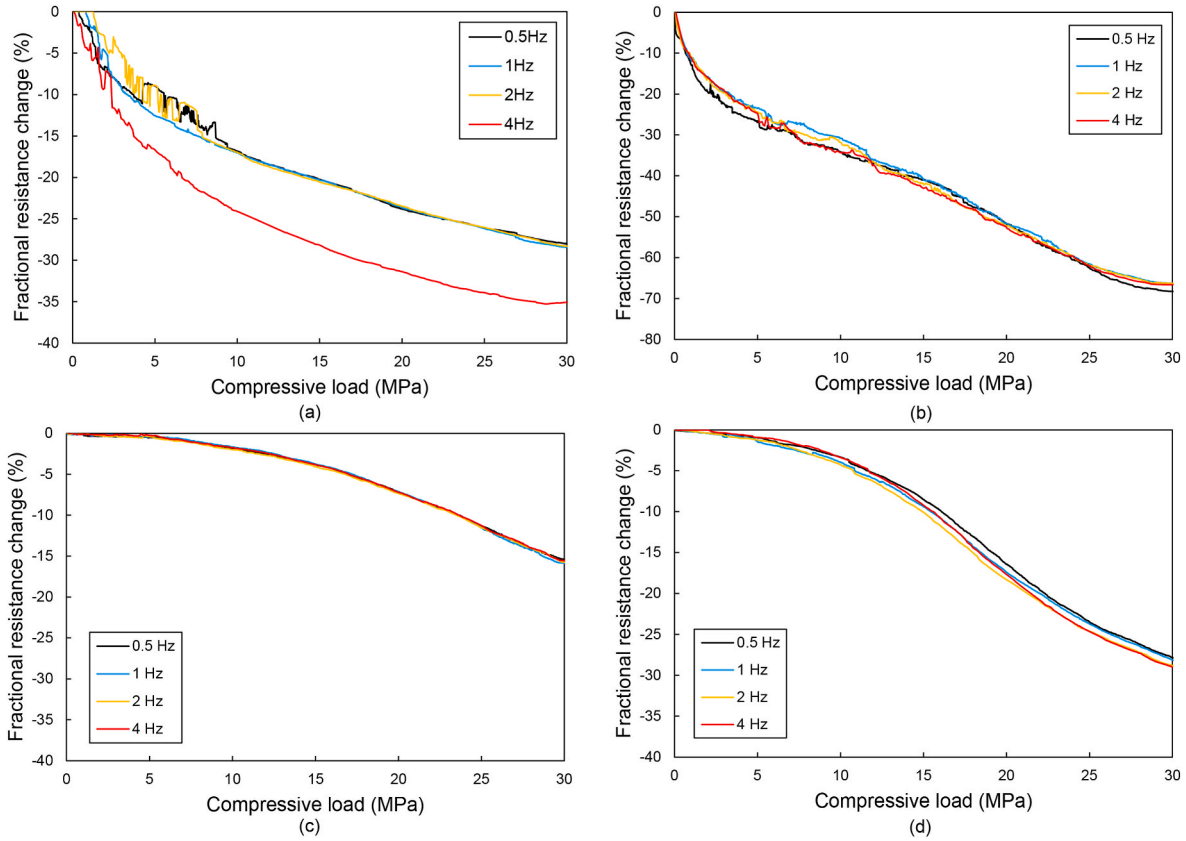

Fig. 16. Fractional resistance change of the samples with TWCNT content of (a) 0.1, (b) 0.2, (c) 0.3, and (d) 0.5% under the monotonic compressive loadings with various loading frequencies.

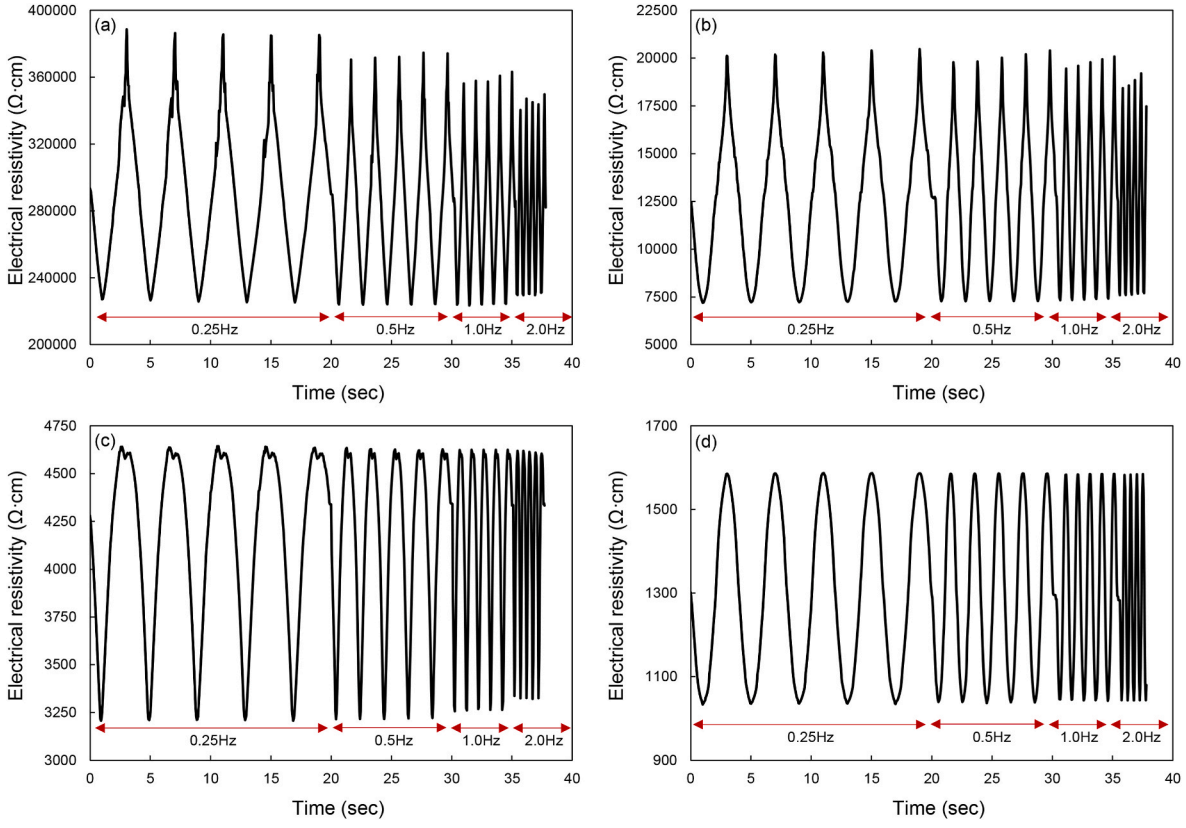

Fig. 17. Electrical resistivity change of the samples with TWCNT content of (a) 0.1, (b) 0.2, (c) 0.3, and (d) 0.5% under the dynamic compressive loadings with various loading frequencies.

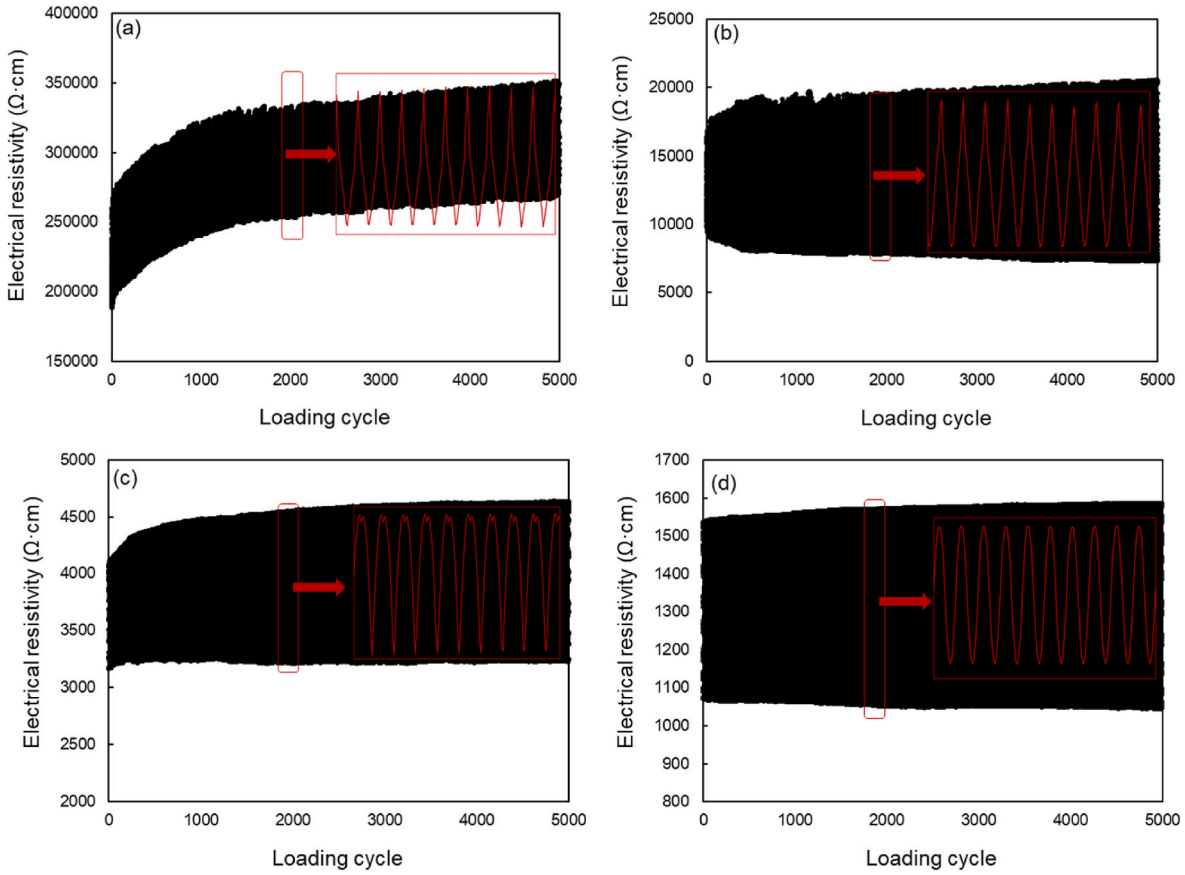

Fig. 18. Long-term electrical resistivity change of the samples with TWCNT content of (a) 0.1, (b) 0.2, (c) 0.3, and (d) 0.5% under 5000 cycles of compressive loading.

lowered the frequency-dependent sensitivity. In addition, a small amount of TWCNTs formed sparse conductive networks, which may not respond accurately to the applied loading with fast frequencies. For these reasons, a more stable FCR value was observed in the samples with comparably larger amounts of TWCNT contents (i.e., the samples with TWCNT contents of 0.3 and 0.5%).

The electrical resistivity changes of the samples under dynamic compressive loading at various loading frequencies are shown in Fig. 17. The stability of electrical resistivity under dynamic loading improved as the TWCNT content increased. This result was similar to the findings provided in Fig. 16, indicating that a small amount of TWCNT content (i.e., 0.1 and 0.2%) may not respond to the applied loading. Considering the results shown in Figs. 16 and 17, the TWCNT contents higher than the percolation threshold range (i.e., 0.3 and 0.5%) can improve the stability of piezoresistive sensing performances when the loading with various frequencies was applied, even their sensitivity (expressed as FCR value) decreased as compared to the sample with TWCNT contents near the percolation threshold range.

Meanwhile, the piezoresistive sensing performance of cement-based sensors is vulnerable to continuous dynamic loading because continuous loading can cause the formation of cracks in the sensors, thereby degrading the sensing stability [68]. The long-term electrical resistivity changes of the samples under 5000 cycles of compressive loading are shown in Fig. 18. The electrical resistivity of the samples commonly increased regardless of the TWCNT content as the loading cycles proceeded. Comparably stable electrical resistivity was found after 3000 loading cycles, which was similar to the findings of a previous study [68]. The increase in electrical resistivity during continuous loading was explained by the formation of microcracks in the samples when continuous loading was applied. However, the samples with TWCNT contents of 0.1 and 0.2% showed higher extents of electrical resistivity increase as compared to the samples with TWCNT contents of 0.3 and 0.5%. According to the piezoresistive sensing mechanisms, it was reported that the TWCNT-based conductivity networks was disturbed as

Table 3
Comparison of the measured piezoresistive sensing performances with the test outcomes reported in earlier works [74–80].

Conductive filler (Content (wt% of binder))	Matrix type	Applied stress (MPa)	Stress sensitivity (%/MPa)	Reference
GNP (1.0)	Paste	0–5	1.4	[74]
MWCNT (0.1)	Paste	0–4.2	1.07	[75]
CNF (0.1)			1.26	
GNP (0.05)	UHPC	0–20	1	[76]
MWCNT (0.1)	Paste Mortar Concrete	0–0.8	0.72 0.05 0.04	[77]
GNP (6.4)	Concrete	0–8	1.01	[78]
MWCNT (0.05)	Mortar	1–6	0.23	[79]
MWCNT (0.1)			0.55	
CB (10)	Mortar	0–9.4	0.19	[80]
TWCNT (0.1) (0.2) (0.3) (0.5)	UHPC	0–30	1.40 2.16 1.03 1.16	This study

the continuous loading was applied to the cement-based sensors [68]. In addition, disturbances in TWCNT-based conductive networks caused disconnections between adjacent TWCNTs, thereby increasing the electrical resistivity [69]. This explanation was reflected in the samples with small TWCNT contents because the small changes in electrical resistivity affects the dramatic change in the FCR value in the samples with small TWCNT contents, while it was not notable in the samples with high TWCNT contents.

Table 3 provides the comparison of the measured piezoresistive sensing performances with the test outcomes reported in earlier works using various conductive fillers. The sensitivity values obtained by this study were found to be comparable to or superior to the test outcomes reported in earlier works. In addition, the stress sensitivity value calculated in this study was found to the highest at the TWCNT content near that exhibited the percolation threshold, showing an improved sensitivity than those of cement-based sensors containing similar conductive filler contents. In particular, the applied stress levels used in this study (i.e., 0–50 MPa) were broader than those used in earlier works. Therefore, the cement-based sensors developed in this study can be regarded to accommodate a broad range of applicability and potential for the practical introduction [21,72–74].

To date, most researchers have fabricated CNT-embedded cementitious composites and attempted to achieve a higher sensitivity [24,67–71,81]. They reported that a CNT amount in the percolation threshold range was suitable for fabricating cement-based sensors with high sensitivity [24,67–71,81]. However, they investigated the sensing capabilities without considering various dynamic conditions in detail. As seen in the test results provided in this study, the addition of TWCNT content higher than the percolation threshold level improved the sensing stability considering various dynamic loading conditions and exposure environmental conditions. Based on these perspectives, further studies on the long-term sensing stability and durability of the fabricated TWCNT-embedded UHPC exposed to various environmental parameters must be conducted.

5. Conclusion

The present study performed material characterization of TWCNT-embedded UHPC samples and evaluated their piezoresistive sensing capabilities. The UHPC samples with various TWCNT contents were fabricated, and their fresh and hardened physicochemical properties were investigated by table flow tests, setting time measurements, XRD, solid-state ^{29}Si NMR spectroscopy, SEM, strength tests, and MIP. The piezoresistive sensing properties of the samples were examined using electrical resistivity measurements and FCR values upon monotonic and dynamic loading conditions. Finally, the long-term sensing capabilities of the samples were assessed under 5000 cycles of compressive loading. The following conclusions were drawn from this study:

(1) Table flow and setting time of the samples decreased as the TWCNT content increased, especially more severe in the samples with TWCNT content of 0.3 and 0.5%.
(2) The hydration of the samples benefited from the occurrence of the nucleation effect up to TWCNT contents of 0.2–0.3%, yet the TWCNTs content exceeding this range adversely influenced the progress of hydration.
(3) Despite the differences in the hydration kinetics with different TWCNT contents, the autogenous shrinkage of the samples was proportionally reduced with an increase in TWCNT content due to hindered hydration and the nano-reinforcing effect.
(4) ^{29}Si NMR revealed that the incorporated TWCNT altered the hydration degree of cement and increased the Al uptake of C-(A)-S-H. However, the compressive and flexural strengths of the samples with TWCNTs at 28 d of curing were not significantly degraded as compared to the sample without TWCNTs.
(5) The electrical resistivities of the samples were notably reduced at TWCNT contents of 0.1–0.2%, indicating that the percolation threshold was found in this TWCNT range. This was shown by the notable variations in the FCR in the sample with a TWCNT content of 0.2% upon cyclic loading tests.
(6) The incorporation of TWCNTs exceeding the percolation threshold (>0.2%) in UHPC which exhibited stable FCR values regardless of the extent of the compressive loading, loading frequency, or number of cycles.

Securing fair mechanical properties and durability performances of TWCNT-embedded cementitious composites is a critical challenge and ultimate goal in order for one to utilize these composites within a long-range timeframe. Against this backdrop, the introduction of UHPC to embrace the TWCNT can possibly satisfy the development of high mechanical properties, simultaneously rendering the functionality resulting from the incorporation of TWCNT. These aspects were proven to a certain extent by the outcomes provided in this study, however, the piezoresistive sensing capabilities of the TWCNT-embedded UHPC upon exposure to various and complex harsh conditions should be dealt with further.

CRediT authors' statement

Joonho Seo: Conceptualization, Methodology, Formal analysis, Investigation, Writing - Original Draft, Writing - Review & Editing **Deaik Jang:** Formal analysis, Investigation, Writing - Original Draft, Writing - Review & Editing **Beomjoo Yang:** Formal analysis, Investigation, Writing - Review & Editing **H.N. Yoon:** Investigation, Writing - Review & Editing **Jeong Gook Jang:** Formal analysis, Investigation, Writing - Review & Editing, Funding acquisition **Solmoi Park:** Formal analysis, Investigation, Writing - Review & Editing **H.K. Lee:** Investigation, Writing - Review & Editing, Project administration, Funding acquisition.

Declaration of competing interest

The authors declare that they have no known competing financial interests or personal relationships that could have appeared to influence the work reported in this paper.

Data availability

Data will be made available on request.

Acknowledgments

This study was supported by the National Research Foundation (NRF) of the Korean government (Ministry of Science & ICT) [No. 2021R1A2C3006382]. This study was also supported by a grant (21CTAP-C163988-01) from Ministry of Land, Infrastructure and Transport (MOLIT) of Korea government and Korea Agency for Infrastructure Technology Advancement (KAIA). The authors would like to acknowledge the use of high-resolution XRD at KBSI Daegu Center. The authors would like to thank Dr. S.J. Lee for assistance with Particle and Pore size Analysis System at KBSI Jeonju Center. The authors also acknowledge the use of the solid-state NMR spectrometer at the Korea Basic Science Institute Western Seoul Center.

References

[1] K. Wille, A.E. Naaman, G.J. Parra-Montesinos, Ultra-high performance concrete with compressive strength exceeding 150 MPa (22 ksi): a simpler way, ACI Mater. J. 108 (2011).
[2] K. Habel, M. Viviani, E. Denarié, E. Brühwiler, Development of the mechanical properties of an ultra-high performance fiber reinforced concrete (UHPFRC), Cement Concr. Res. 36 (2006) 1362–1370.

[3] P. Richard, M. Cheyrezy, Composition of reactive powder concretes, Cement Concr. Res. 25 (1995) 1501–1511.
[4] J. Du, W. Meng, K.H. Khayat, Y. Bao, P. Guo, Z. Lyu, A. Abu-obeidah, H. Nassif, H. Wang, New development of ultra-high-performance concrete (UHPC), Compos. B Eng. 224 (2021), 109220.
[5] A.C. 239, Ultra-high-performance Concrete: an Emerging Technology Report, American Concrete Institute, 2018. ACI 239R-18).
[6] V. Perry, What really is ultra-high performance concrete?–Towards a global definition, in: The 2nd International Conference on Ultra-high Performance Concrete Material & Structures, 2018, pp. 7–10.
[7] Y. Li, T. Mi, W. Liu, Z. Dong, B. Dong, L. Tang, F. Xing, Chemical and mineralogical characteristics of carbonated and uncarbonated cement pastes subjected to high temperatures, Compos. B Eng. 216 (2021), 108861.
[8] B.A. Graybeal, Flexural behavior of an ultrahigh-performance concrete I-girder, J. Bridge Eng. 13 (2008) 602–610.
[9] N. Xie, X. Shi, D. Feng, B. Kuang, H. Li, Percolation backbone structure analysis in electrically conductive carbon fiber reinforced cement composites, Compos. B Eng. 43 (2012) 3270–3275.
[10] B. Han, L. Zhang, C. Zhang, Y. Wang, X. Yu, J. Ou, Reinforcement effect and mechanism of carbon fibers to mechanical and electrically conductive properties of cement-based materials, Construct. Build. Mater. 125 (2016) 479–489.
[11] I.W. Nam, H.-K. Lee, Synergistic effect of MWNT/fly ash incorporation on the EMI shielding/absorbing characteristics of cementitious materials, Construct. Build. Mater. 115 (2016) 651–661.
[12] D. Jang, H. Yoon, J. Seo, S. Park, T. Kil, H.-K. Lee, Improved electric heating characteristics of CNT-embedded polymeric composites with an addition of silica aerogel, Compos. Sci. Technol. 212 (2021), 108866.
[13] H. Tohidi, S. Hosseini-Hashemi, A. Maghsoudpour, Size-dependent forced vibration response of embedded micro cylindrical shells reinforced with agglomerated CNTs using strain gradient theory, Smart Struct. Syst. 22 (2018) 527–546.
[14] B. Han, X. Yu, E. Kwon, A self-sensing carbon nanotube/cement composite for traffic monitoring, Nanotechnology 20 (2009), 445501.
[15] D. Jang, H. Yoon, B. Yang, J. Seo, S.Z. Farooq, H.-K. Lee, Synergistic effects of CNT and CB inclusion on the piezoresistive sensing behaviors of cementitious composites blended with fly ash, Smart Struct. Syst. 29 (2022) 351–359.
[16] M. Jung, Y.-s. Lee, S.-G. Hong, J. Moon, Carbon nanotubes (CNTs) in ultra-high performance concrete (UHPC): dispersion, mechanical properties, and electromagnetic interference (EMI) shielding effectiveness (SE), Cement Concr. Res. 131 (2020), 106017.
[17] M. Jung, J. Park, S.-g. Hong, J. Moon, Electrically cured ultra-high performance concrete (UHPC) embedded with carbon nanotubes for field casting and crack sensing, Mater. Des. 196 (2020), 109127.
[18] M. Jung, J.-s. Park, S.-G. Hong, J. Moon, Micro-and meso-structural changes on electrically cured ultra-high performance fiber-reinforced concrete with dispersed carbon nanotubes, Cement Concr. Res. 137 (2020), 106214.
[19] D.K. Hardy, M.F. Fadden, M.J. Khattak, A. Khattab, Development and characterization of self-sensing CNF HPFRCC, Mater. Struct. 49 (2016) 5327–5342.
[20] B. Han, L. Zhang, S. Sun, X. Yu, X. Dong, T. Wu, J. Ou, Electrostatic self-assembled carbon nanotube/nano carbon black composite fillers reinforced cement-based materials with multifunctionality, Compos. Appl. Sci. Manuf. 79 (2015) 103–115.
[21] W. Dong, W. Li, Y. Guo, F. Qu, K. Wang, D. Sheng, Piezoresistive performance of hydrophobic cement-based sensors under moisture and chloride-rich environments, Cement Concr. Compos. 126 (2022), 104379.
[22] D.-Y. Yoo, I. You, S.-J. Lee, Electrical properties of cement-based composites with carbon nanotubes, graphene, and graphite nanofibers, Sensors 17 (2017) 1064.
[23] X. Yu, E. Kwon, A carbon nanotube/cement composite with piezoresistive properties, Smart Mater. Struct. 18 (2009), 055010.
[24] I. Nam, H. Souri, H.-K. Lee, Percolation threshold and piezoresistive response of multi-wall carbon nanotube/cement composites, Smart Struct. Syst. 18 (2016) 217–231.
[25] H. Kim, I. Park, H.-K. Lee, Improved piezoresistive sensitivity and stability of CNT/cement mortar composites with low water–binder ratio, Compos. Struct. 116 (2014) 713–719.
[26] M. Jung, S.-g. Hong, J. Moon, Ozone treatment on the dispersion of carbon nanotubes in ultra-high performance concrete, Mater. Des. 193 (2020), 108813.
[27] Z. Chen, J.L.G. Lim, E.-H. Yang, Ultra high performance cement-based composites incorporating low dosage of plasma synthesized carbon nanotubes, Mater. Des. 108 (2016) 479–487.
[28] M. Jung, J. Park, S.-g. Hong, J. Moon, The critical incorporation concentration (CIC) of dispersed carbon nanotubes for tailoring multifunctional properties of ultra-high performance concrete (UHPC), J. Mater. Res. Technol. 17 (2022) 3361–3370.
[29] C. ASTM, Standard Test Method for Flow of Hydraulic Cement Mortar, 2007, p. C1437.
[30] C. ASTM, 191-08, Standard Test Methods for Time of Setting of Hydraulic Cement by Vicat Needle, ASTM International, West Conshohocken, PA, 2008.
[31] J. Seo, S. Kim, S. Park, S. Bae, H.-K. Lee, Microstructural evolution and carbonation behavior of lime-slag binary binders, Cement Concr. Compos. 119 (2021), 104000.
[32] D. Jang, H. Yoon, S. Farooq, H.-K. Lee, I. Nam, Influence of water ingress on the electrical properties and electromechanical sensing capabilities of CNT/cement composites, J. Build. Eng. 42 (2021), 103065.
[33] Y. Wang, X. Zhao, Y. Zhao, Piezoresistivity of cement matrix composites incorporating multiwalled carbon nanotubes due to moisture variation, Adv. Civ. Eng. (2020) 2020.
[34] O.A.M. Reales, Y.P.A. Jaramillo, J.C.O. Botero, C.A. Delgado, J.H. Quintero, R. D. Toledo Filho, Influence of MWCNT/surfactant dispersions on the rheology of Portland cement pastes, Cement Concr. Res. 107 (2018) 101–109.
[35] F. Collins, J. Lambert, W.H. Duan, The influences of admixtures on the dispersion, workability, and strength of carbon nanotube–OPC paste mixtures, Cement Concr. Compos. 34 (2012) 201–207.
[36] G. Kim, I. Nam, B. Yang, H. Yoon, H.-K. Lee, S. Park, Carbon nanotube (CNT) incorporated cementitious composites for functional construction materials: the state of the art, Compos. Struct. 227 (2019), 111244.
[37] S. Yousef, R. Kalpokaitė-Dičkuvienė, A. Baltušnikas, I. Pitak, S.I. Lukošiūtė, A new strategy for functionalization of char derived from pyrolysis of textile waste and its application as hybrid fillers (CNTs/char and graphene/char) in cement industry, J. Clean. Prod. 314 (2021), 128058.
[38] Y. Du, J. Yang, B.S. Thomas, L. Li, H. Li, W.M. Shaban, W.T. Chong, Influence of hybrid graphene oxide/carbon nanotubes on the mechanical properties and microstructure of magnesium potassium phosphate cement paste, Construct. Build. Mater. 260 (2020), 120449.
[39] J. Makar, J. Margeson, J. Luh, Carbon nanotube/cement composites-early results and potential applications, in: Proceedings of the 3rd International Conference on Construction Materials: Performance, Innovations and Structural Implications, Vancouver Canada, 2005, pp. 1–10.
[40] J.M. Makar, G.W. Chan, Growth of cement hydration products on single-walled carbon nanotubes, J. Am. Ceram. Soc. 92 (2009) 1303–1310.
[41] T. Manzur, N. Yazdani, M. Emon, A. Bashar, Potential of carbon nanotube reinforced cement composites as concrete repair material, J. Nanomater. (2016) 2016.
[42] H. Cui, S. Yang, S.A. Memon, Development of carbon nanotube modified cement paste with microencapsulated phase-change material for structural–functional integrated application, Int. J. Mol. Sci. 16 (2015) 8027–8039.
[43] Ç. Yalçınkaya, O. Çopuroğlu, Hydration heat, strength and microstructure characteristics of UHPC containing blast furnace slag, J. Build. Eng. 34 (2021), 101915.
[44] K.L. Scrivener, P. Juilland, P.J. Monteiro, Advances in understanding hydration of Portland cement, Cement Concr. Res. 78 (2015) 38–56.
[45] O.A.M. Reales, P.A. Carisio, T.C. dos Santos, W.C. Pearl Jr., R.D. Toledo Filho, Effect of pozzolanic micro and nanoparticles as secondary fillers in carbon nanotubes/cement composites, Construct. Build. Mater. 281 (2021), 122603.
[46] U. EPA, in: E.P. Agency (Ed.), Method 1311 Toxicity Characteristic Leaching Procedure (TCLP), 1992, p. USA1992. Washington DC.
[47] G. Kim, H. Yoon, H.-K. Lee, Autogenous shrinkage and electrical characteristics of cement pastes and mortars with carbon nanotube and carbon fiber, Construct. Build. Mater. 177 (2018) 428–435.
[48] S. Chatterji, J. Jeffery, The volume expansion of hardened cement paste due to the presence of “dead-burnt” CaO, Mag. Concr. Res. 18 (1966) 65–68.
[49] J. Seo, S. Park, H.N. Yoon, H.-K. Lee, Effect of CaO incorporation on the microstructure and autogenous shrinkage of ternary blend Portland cement-slag-silica fume, Construct. Build. Mater. 249 (2020), 118691.
[50] P. Hewlett, M. Liska, Lea's Chemistry of Cement and Concrete, Butterworth-Heinemann, 2019.
[51] J.A. Oates, Lime and Limestone: Chemistry and Technology, Production and Uses, John Wiley & Sons, 2008.
[52] E. Ghafari, S.A. Ghahari, H. Costa, E. Júlio, A. Portugal, L. Durães, Effect of supplementary cementitious materials on autogenous shrinkage of ultra-high performance concrete, Construct. Build. Mater. 127 (2016) 43–48.
[53] F. Blandine, K. Habermehi-Cwirzen, A. Cwirzen, Contribution of CNTs/CNFs morphology to reduction of autogenous shrinkage of Portland cement paste, Front. Struct. Civ. Eng. 10 (2016) 224–235.
[54] C.-M. Aldea, F. Young, K. Wang, S.P. Shah, Effects of curing conditions on properties of concrete using slag replacement, Cement Concr. Res. 30 (2000) 465–472.
[55] S. Greenberg, Reaction between silica and calcium hydroxide solutions. I. Kinetics in the temperature range 30 to 85, J. Phys. Chem. 65 (1961) 12–16.
[56] Y. Qing, Z. Zenan, K. Deyu, C. Rongshen, Influence of nano-SiO2 addition on properties of hardened cement paste as compared with silica fume, Construct. Build. Mater. 21 (2007) 539–545.
[57] J. Seo, S.M. Park, H.-K. Lee, Evolution of the binder gel in carbonation-cured Portland cement in an acidic medium, Cement Concr. Res. 109 (2018) 81–89.
[58] R.J. Myers, E. L'Hôpital, J.L. Provis, B. Lothenbach, Effect of temperature and aluminium on calcium (alumino) silicate hydrate chemistry under equilibrium conditions, Cement Concr. Res. 68 (2015) 83–93.
[59] J. Skibsted, M.D. Andersen, The effect of alkali ions on the incorporation of aluminum in the calcium silicate hydrate (C–S–H) phase resulting from Portland cement hydration studied by 29 Si MAS NMR, J. Am. Ceram. Soc. 96 (2013) 651–656.
[60] N.K. Lee, K. Koh, M.O. Kim, G. Ryu, Uncovering the role of micro silica in hydration of ultra-high performance concrete (UHPC), Cement Concr. Res. 104 (2018) 68–79.
[61] T. Bach, C.C.D. Coumes, I. Pochard, C. Mercier, B. Revel, A. Nonat, Influence of temperature on the hydration products of low pH cements, Cement Concr. Res. 42 (2012) 805–817.
[62] D. Hou, Z. Lu, X. Li, H. Ma, Z. Li, Reactive molecular dynamics and experimental study of graphene-cement composites: structure, dynamics and reinforcement mechanisms, Carbon 115 (2017) 188–208.
[63] H. Alkhateb, A. Al-Ostaz, A.H.-D. Cheng, X. Li, Materials genome for graphene-cement nanocomposites, J. Nanomecch. Micromech. 3 (2013) 67–77.

[64] R.J. Myers, S.A. Bernal, R. San Nicolas, J.L. Provis, Generalized structural description of calcium–sodium aluminosilicate hydrate gels: the cross-linked substituted tobermorite model, Langmuir 29 (2013) 5294–5306.
[65] B. Sindu, S. Sasmal, Multi-scale Abridged cement composite with enhanced mechanical properties, ACI Mater. J. 117 (2020).
[66] B. Sindu, S. Sasmal, On the development and studies of nano-and micro-fiber hybridized strain hardened cementitious composite, Arch. Civ. Mech. Eng. 19 (2019) 348–359.
[67] Z. Wu, C. Shi, K.H. Khayat, L. Xie, Effect of SCM and nano-particles on static and dynamic mechanical properties of UHPC, Construct. Build. Mater. 182 (2018) 118–125.
[68] D. Jang, H. Yoon, J. Seo, B. Yang, Effects of exposure temperature on the piezoresistive sensing performances of MWCNT-embedded cementitious sensor, J. Build. Eng. 47 (2022), 103816.
[69] W. Dong, W. Li, K. Wang, B. Han, D. Sheng, S.P. Shah, Investigation on physicochemical and piezoresistive properties of smart MWCNT/cementitious composite exposed to elevated temperatures, Cement Concr. Compos. 112 (2020), 103675.
[70] S.-J. Lee, I. You, S. Kim, H.-O. Shin, D.-Y. Yoo, Self-sensing capacity of ultra-high-performance fiber-reinforced concrete containing conductive powders in tension, Cement Concr. Compos. 125 (2022), 104331.
[71] W. Dong, W. Li, X. Zhu, D. Sheng, S.P. Shah, Multifunctional cementitious composites with integrated self-sensing and hydrophobic capacities toward smart structural health monitoring, Cement Concr. Compos. 118 (2021), 103962.
[72] W. Li, F. Qu, W. Dong, G. Mishra, S.P. Shah, A comprehensive review on self-sensing graphene/cementitious composites: a pathway toward next-generation smart concrete, Construct. Build. Mater. 331 (2022), 127284.
[73] W. Li, W. Dong, Y. Guo, K. Wang, S.P. Shah, Advances in multifunctional cementitious composites with conductive carbon nanomaterials for smart infrastructure, Cement Concr. Compos. 128 (2022), 104454.
[74] Y. Guo, W. Li, W. Dong, K. Wang, X. He, K. Vessalas, D. Sheng, Self-sensing cement-based sensors with superhydrophobic and self-cleaning capacities after silane-based surficial treatments, Case Stud. Constr. Mater. 17 (2022), e01311.
[75] M.S. Konsta-Gdoutos, C.A. Aza, Self sensing carbon nanotube (CNT) and nanofiber (CNF) cementitious composites for real time damage assessment in smart structures, Cement Concr. Compos. 53 (2014) 162–169.
[76] L. Guo, J. Wu, H. Wang, Mechanical and perceptual characterization of ultra-high-performance cement-based composites with silane-treated graphene nano-platelets, Construct. Build. Mater. 240 (2020), 117926.
[77] A. D'Alessandro, M. Rallini, F. Ubertini, A.L. Materazzi, J.M. Kenny, Investigations on scalable fabrication procedures for self-sensing carbon nanotube cement-matrix composites for SHM applications, Cement Concr. Compos. 65 (2016) 200–213.
[78] Q. Liu, R. Gao, V.W. Tam, W. Li, J. Xiao, Strain monitoring for a bending concrete beam by using piezoresistive cement-based sensors, Construct. Build. Mater. 167 (2018) 338–347.
[79] M. Mardani, S.H.H. Lavassani, M. Adresi, A. Rashidi, Piezoresistivity and mechanical properties of self-sensing CNT cementitious nanocomposites: optimizing the effects of CNT dispersion and surfactants, Construct. Build. Mater. 349 (2022), 128127.
[80] A.O. Monteiro, P.B. Cachim, P.M. Costa, Self-sensing piezoresistive cement composite loaded with carbon black particles, Cement Concr. Compos. 81 (2017) 59–65.
[81] X. Xiong, M. Wu, W. Shen, J. Li, D. Zhao, P. Li, J. Wu, Performance and microstructure of ultra-high-performance concrete (UHPC) with silica fume replaced by inert mineral powders, Construct. Build. Mater. 327 (2022), 126996.